Cryo-ET reveals nucleosome reorganisation in condensed mitotic chromosomes *in vivo*

Shujun Cai[1], Chen Chen[1], Zhi Yang Tan[1], Yinyi Huang[2,†], Jian Shi[1] and Lu Gan[1]*

[1] Department of Biological Sciences and Centre for BioImaging Sciences, National University of Singapore, Singapore 117543

[2] Temasek Life Sciences Laboratory, National University of Singapore, Singapore 117604

[†] Present address: School of Life Sciences & Chemical Technology, Ngee Ann Polytechnic, Singapore 599489

* Correspondence: lu@anaphase.org

SUMMARY

Chromosomes condense during mitosis in most eukaryotes. This transformation involves rearrangements at the nucleosome level and has consequences for transcription, but the details remain unclear. Here, we use cryo-electron tomography to determine the 3-D arrangement of nucleosomes and other large nuclear features in frozen-hydrated fission-yeast cells. Nucleosomes can form irregular clusters in both interphase and mitotic cells, but they are smaller than expected for Hi-C domains. The nucleosomes are co-mingled with two features: nucleosome-free pockets and megadalton-sized “megacomplexes”. Compared to interphase, the nucleosomes in mitotic chromosomes pack into slightly larger clusters. However, nearest-neighbor distance analysis reveals that mitotic nucleosome clusters have the same internal packing density as in interphase. Furthermore, mitotic chromosomes contain fewer megacomplexes. This uneven chromosome condensation helps explain a longstanding enigma of mitosis: most genes are repressed but a subset is upregulated.

INTRODUCTION

Chromatin structure influences key nuclear activities such as transcription, DNA repair and replication (Dixon et al., 2016). The fundamental unit of chromatin is the nucleosome, which consists of ~147 bp of DNA wrapped around a histone octamer Luger, 1997]. In mammalian cells, 2 - 35 nucleosomes pack into irregular “clutches” (Ricci et al., 2015) and more than 500 nucleosomes (calculated from nucleosome spacing) are thought to associate as topologically associating domains (Dixon et al., 2012). Likewise, in the fission yeast *Schizosaccharomyces pombe*, some 300 - 7,000 nucleosomes are thought to associate as compact globular chromatin bodies called domains (Mizuguchi et al., 2014; Kakui et al., 2017; Tanizawa et al., 2017). These studies suggest that chromatin higher-order structure arises from physical interactions of large groups of nucleosomes.

In mitotic cells, chromosomes condense into discrete structures that can be resolved in a light microscope. The factors involved in condensation have been well characterized (Hirano, 2016) and a number of models have been proposed for the large-scale organisation of chromatin domains (Maeshima and Eltsov, 2008). However, the molecular details of chromatin reorganisation are still unknown. Knowledge of how chromatin condenses in 3-D at the single-nucleosome level is needed to explain the nearly global transcriptional repression that happens to the mitotic cells of most eukaryotes (Struhl, 1998). Likewise, a 3-D model of chromatin could also explain how a subset of genes escape this mitotic repression and get upregulated (Rustici et al.; Oliva et al.; Peng et al.).

Some insights on *in vivo* chromatin organisation were made possible by new methods, including chromatin-conformation capture (Hi-C), super-resolution microscopy, and traditional EM of cells stained with DNA-proximal osmium (Beliveau et al.; Pombo and Dillon, 2015; Ou et al.). However, the resultant models are limited because these methods rely on population-averaged data, or have low resolution, or perturb the sample due to the fixation, dehydration and staining. Cryo-EM is a label-free method to visualize cells in a life-like frozen-hydrated state (McDowall et al., 1986; Eltsov et al., 2008). Cryo-electron tomography (cryo-ET) goes further and can reveal the 3-D positions of these complexes at ~ 4-nm resolution (Gan and Jensen, 2012). Using cryo-ET, we previously showed that nucleosomes in picoplankton and budding yeast pack irregularly, but we did not find evidence for mitotic chromosome compaction (Gan et al., 2013; Chen et al., 2016).

Fission-yeast mitotic-chromosome condensation resembles human chromosome condensation in both morphological and Hi-C phenotypes (Hiraoka et al., 1984; Naumova et al., 2013; Yam et al., 2013; Kakui et al., 2017; Tanizawa et al., 2017). We have now used cryo-ET to directly visualize chromatin both before and after mitotic condensation *in vivo* in the fission yeasts *S. pombe* and *S. japonicus*. To obtain cryotomograms with sufficient contrast to resolve nucleosomes *in vivo*, we imaged cells that were thinned by cryomicrotomy. To better understand the heterogeneous complexes in the crowded nucleoplasm, we also took advantage of recent advances in phase-contrast hardware and image-classification software (Bharat and Scheres, 2016; Khoshouei et al., 2017). We found that in interphase, nucleosomes frequently associate as small clusters or short chains. Nucleosome-free pockets and megadalton-sized

82 “megacomplexes” are interspersed among these nucleosome clusters. In mitosis,
83 chromosomes condense unevenly and have slightly larger nucleosome clusters. Mitotic
84 chromosomes also have nucleosome-free pockets, but fewer megacomplexes. These
85 phenotypes are conserved in both types of fission yeasts and lead to a model that
86 explains how some genes can be transcriptionally upregulated in mitosis.

RESULTS

S. pombe subcellular structures are revealed at molecular resolution by cryo-ET

To understand how native chromatin organisation differs between interphase and mitosis, we imaged *S. pombe* cells by cryo-ET of frozen-hydrated sections (cryosections, ~ 90 - 130 nm nominal thickness). To ensure that the imaged cells had a known cell-cycle state, we arrested temperature-sensitive *cdc25-22* cells in G2 phase (Fantes, 1979) and cold-sensitive *nda3-KM311* cells in prometaphase (Hiraoka et al., 1984). Fluorescence microscopy confirmed that the latter cells have the well-known mitotic chromosome-condensation phenotype (Fig. 1A, S1). In a typical cryotomogram of an *S. pombe* cell, we could recognize organelles such as the endoplasmic reticulum, vesicles, and the nucleus due to their membrane morphologies (Fig. 1B and C). To further assess the quality of the cryosections and data, we performed subtomogram averaging of cytoplasmic ribosomes (Fig. S2A, B). The resulting average was similar to a low-pass-filtered budding-yeast ribosome crystal structure (Fig. S1C) (Ben-Shem et al., 2011). Therefore, the conformation of large complexes are preserved at the molecular level.

Interphase chromatin is arranged as loosely packed nucleosomes and irregular nucleosome clusters

G2-phase cell nuclei are filled with many nucleosome-like granular densities. For the sake of brevity, herein we call these densities nucleosomes due to their size, shape, abundance, location, and condensation phenotype all being consistent with

nucleosomes (see below). Even if a minority of these densities are not nucleosomes, the conclusions we make below are still valid. Nucleosomes frequently associate as small irregular clusters less than 50-nm wide (Fig. 2B). Chain-like nucleosome configurations are also abundant (Fig. 2C). *S. pombe* linker DNA is only 7-bp, corresponding to ~ 2.5 nm (Lantermann et al., 2010), meaning that most nucleosomes should pack closely with at least two other nucleosomes. These two nucleosomes correspond to the -1 and +1 positions in the sequence. Because linker DNA is unresolved in our cryotomograms, we do not know if a cluster contains nucleosomes from a single or multiple sequences of nucleosomes. The remaining nucleosomes are not clustered together (Fig. 2D). Efforts to automatically identify nucleosome clusters with distinct motifs failed due to the irregular nucleosome packing. Small nucleosome-free "pockets" (< 50 nm) are also abundant (Fig. 2E). Densities much larger than nucleosomes (> 20 nm) are spread throughout the nucleus (Fig. 2F). These densities are consistent with being multi-megadalton nuclear assemblies such as pre-ribosomes, spliceosomes, and transcription preinitiation complexes (Gleizes et al., 2001; Allen and Taatjes, 2015; Oesterreich et al., 2016); we call these "megacomplexes" for brevity. Therefore, in interphase, nucleosomes associate as small irregular clusters that co-mingle with megacomplexes and nucleosome-free pockets.

Condensed mitotic chromosomes contain fewer megacomplexes

Unlike in G2-phase cells, in each cryotomogram of a prometaphase cell we found a single position that has many features consistent with its being a section through a condensed chromosome. For example, nucleosome-like densities are abundant within

these positions, but much rarer outside (Fig. 3A-C). Compared to G2-phase cells, in which abundant megacomplexes are interspersed with the chromatin (Fig. 2A), megacomplexes are mostly absent from these large contiguous regions in prometaphase cells (Fig. 3A). These positions are hundreds of nanometers wide, matching the size of condensed chromosomes seen by fluorescence microscopy (Fig. 1A, S1). If these positions are indeed chromosomes, there should be a large contiguous volume in the cell with few megacomplexes. To test this hypothesis, we sampled a larger nuclear volume by cryo-ET of 5 nearly sequential cryosections (summing to ~ 700 nm thick) of the same cell (Fig. S3A). We saw a single megacomplex-poor region in each of these cryosections, which is consistent with these positions being sections through one or two of the three fission-yeast chromosomes (Fig. S3B-F). Taken together, we located mitotic chromosomes and found they have fewer megacomplexes within.

Mitotic chromosomes condense unevenly and support transcription

In conventional (defocus) cryotomograms, we noticed that most nucleosomes appear more densely packed in prometaphase cells (Fig. S4). To better understand how chromatin is organised, we imaged cells by Volta phase contrast cryo-ET (Fig. S5). Volta cryo-EM data have much more contrast, making it possible to locate and determine the orientations of smaller protein complexes and to resolve protein complexes packed to near-crystalline density inside of cells (Engel et al., 2015; Khoshouei et al., 2017). The Volta cryotomograms confirmed what we learned from defocus cryo-ET: prometaphase nucleosomes more frequently packed into larger

clusters (Figs. 4A and B, S5). Importantly, we confirmed the presence of some loosely packed nucleosomes and pockets in prometaphase cells (Figs. 4C and S5B, D), meaning that condensation is uneven. In summary, mitotic chromosomes consist of both densely and loosely packed nucleosomes.

The existence of loosely packed nucleosomes in prometaphase cells suggests that mitotic chromatin is permissive to transcriptional machinery, which is supported by the observation that some genes are up-regulated during mitosis (Rustici et al., 2004; Oliva et al., 2005; Peng et al., 2005). However, these earlier studies could not determine if *S. pombe* undergoes active mitotic RNA polymerase II transcription or if some stable mRNAs are left over from G2 phase. Phosphorylation of RNA polymerase II at Serine 2 of the carboxy-terminal domain (CTD) heptamer repeat is a conserved marker of transcription elongation (Komarnitsky et al., 2000; Harlen and Churchman, 2017). Using immunofluorescence, we confirmed the existence of RNA polymerase II with phospho-Ser2 CTD, and therefore active transcription, in prometaphase chromosomes (Fig. S6). To rule out the possibility of abnormal transcriptional activity in the mutants, we imaged asynchronous wild-type cultures, in which a small minority of cells was undergoing mitosis. We also detected phospho-Ser2 CTD signal in both early and late mitotic cells. Therefore, transcription is not shut-down globally in mitotic *S. pombe* cells.

To analyse the nucleosome rearrangement more objectively, we performed template matching to find their 3-D positions in Volta cryotomograms. This analysis showed that nucleosomes formed clusters in both G2-phase and prometaphase cells, but appear more crowded in the latter (Fig. 5A, B). If chromosomes condense via a

uniform accretion of all nucleosomes, the average nucleosome nearest-neighbor distance (NND) distribution should shorten. However, the NND distributions of nucleosome hits in G2-phase and prometaphase cells were indistinguishable (two-tailed t-test, $p > 0.05$) (Fig. 5C). While mitotic chromatin might not condense by compaction of nearest-neighbor nucleosomes, they might instead condense from changes in interactions between groups of nucleosomes. We tested this hypothesis by creating histograms of 10^{th} NNDs and found that the population shifted to shorter distances in prometaphase cells (two-tailed t-test, $p < 0.001$) (Fig. 5D), which explains the more-crowded appearance of prometaphase nucleosomes. Taken together, our analyses reveal that chromosomes condense by the merging of small nucleosome clusters, resulting in a closer association between distant nucleosomes (Fig. 5E, F).

As an alternative approach to studying nucleosomes *in vivo*, we performed cryo-ET on the undigested chromatin from lysates of G2-phase and prometaphase *S. pombe* cells. Cryotomograms of cell lysis products can reveal more clearly the positions of nucleosomes (Cai et al., 2017). Subtomogram averages of nucleosome template-matching hits revealed unambiguous features of mononucleosomes including the groove between two DNA gyres (Fig. S7), demonstrating that our template-matching approach can locate most nucleosomes. In the lysates, there are many large nucleosome-free pockets wider than 50 nm in G2-phase chromatin. In contrast, prometaphase chromatin remained as more-compact masses with only a few, smaller pockets (Fig. S8). Therefore, prometaphase chromatin has denser nucleosome packing both *in vivo* and *in vitro*.

***S. japonicus* and *S. pombe* chromosomes condense by similar means**

To test whether the formation of larger nucleosome clusters during condensation is conserved, we imaged *S. japonicus*, a bigger fission yeast that also undergoes mitotic condensation (Robinow and Hyams, 1989). *S. japonicus* has the same genome size (~ 12Mb) as *S. pombe*, but has a nucleus at least 8-fold more voluminous. Because *S. japonicus* is a less-developed model organism, we used asynchronous wild-type cells. These cells were frozen, cryosectioned, and subjected to Volta cryo-ET just like for *S. pombe*. To determine whether a cell was in mitosis or interphase at the time of freezing, we looked for cells with cytoplasmic microtubules, which exist only in interphase, or cells with nuclear microtubules, which exist only in mitosis (Yam et al., 2013). We found densely packed nucleosomes in *S. japonicus* mitotic chromosomes (Fig. S9A-D). Furthermore, NND and 10th-NND analyses showed that the nucleosome NND distributions were similar in interphase and mitosis (two-tailed t-test, $p > 0.05$), but that the 10th-NND distribution was shorter in mitosis (two-tailed t-test, $p < 0.001$) (Fig. S9E, F). Therefore, the formation of larger nucleosome clusters in mitosis is a conserved phenotype in fission yeasts.

Dinucleosomes are irregular *in vivo*

The crowded nature of the nucleus makes it unfeasible to manually search for reproducible nucleosome-packing motifs. We therefore performed reference-free 2-D class-averaging analysis on di-nucleosomes extracted from our cryotomograms. Our previous 2-D classification of natural *S. cerevisiae* chromatin *in vitro* showed that abundant motifs can be found automatically this way (Cai et al., 2017). For example,

pairs of nucleosomes sometimes packed face-to-face *in vitro*, which if present *in vivo* would limit access to regulatory positions like the acidic patch (Luger et al., 1997). However, the same analysis of di-nucleosomes in *S. pombe* did not reveal any classes containing face-to-face-packed nucleosomes (Fig. S10), meaning that such inter-nucleosome interactions must be extremely rare. Instead, di-nucleosomes were packed irregularly, including edge-to-edge packing, with ~ 3-nm gaps in between. G2-phase nucleosomes (Fig. S10A and C) were more irregularly packed in terms of the separation between candidate nucleosomes than in prometaphase cells (Fig. S10B and D). Taken together, our 2-D classification analyses did not find evidence of ordered nucleosome packing *in vivo*.

A subset of nucleosomes may be partially unwrapped

In a rare instances, we were able to resolve densities that resemble linker DNA spanning two nucleosome-like densities in *S. pombe* G2-phase chromatin (Fig. S11A, B). Many of these linker-DNA-like densities were much longer than the average ~ 2 nm expected from MNase-digestion experiments (Fig. S11C-D) and nucleosome-mapping studies (Lantermann et al., 2010). Furthermore, in the NND analysis, there are a large number of nucleosome pairs that have NND values greater than 12 nm, i.e., the gaps between adjacent nucleosomes are wider than 2 nm (Fig. 5C). This inter-nucleosome gap was absent from tetranucleosomes reconstituted with the same linker DNA length as *S. pombe* (Ekundayo et al., 2017). One explanation is that the larger inter-nucleosome separation *in vivo* reflects the high end of the distribution of linker DNA lengths. Alternatively, some nucleosomes might be partially unwrapped – such as may

be expected of fragile or pre-nucleosomes (Fei et al., 2015; Kubik et al., 2015), resulting in apparently longer linker DNA (Fig. S11E, F). The possibility of partially unwrapped nucleosomes led us to test whether the nucleosomes *in vivo* resembled mononucleosomes. To do this, we performed 2-D and 3-D classification of nucleosome template-matching hits (Bharat and Scheres, 2016). The 3-D classes taken from the Volta cryotomograms had the correct size and shape of nucleosomes, but they lacked the characteristic DNA gyres seen in the side view of the low-pass-filtered crystal structure of the mononucleosome (Fig. S12) (Luger et al., 1997). This difference might be due to either the insufficient signal-to-noise ratio of cryo-ET data or the conformational heterogeneity caused by biological factors such as partial unwrapping or both.

DISCUSSION

We have directly visualized chromatin in both interphase and mitotic fission-yeast cells by cryo-ET. The condensation phenotypes are subtle. In both interphase and mitotic cells, most of the nucleosomes are packed into small irregular clusters. While the nucleosome clusters are slightly larger in mitosis, the nearest-neighbor distance does not shorten. In other words, there is no wholesale nucleosome accretion as commonly depicted in textbooks. The most notable -- yet still subtle -- changes are that mitotic chromatin contains fewer megacomplexes *in vivo* and that this chromatin remains more compact than interphase chromatin after being released from lysed cells. We propose a model of mitotic condensation that incorporates both structural and dynamic principles that takes into account recently published counter-intuitive Hi-C results (Fig. 6).

Cryo-ET reveals new insights into higher-order chromatin organisation

One of the long-standing goals of structural cell biology is to determine how a chain of sequential nucleosomes folds within minimally perturbed cells. Such a model requires the visualization of all the linker-DNA segments, but cryo-ET at present can resolve only a tiny minority of this DNA *in vivo*. Despite this limitation, the shortness of fission-yeast linker DNA (Fig. S10) tightly constrains our interpretation of our cryotomograms. Any given nucleosome density should have at least two adjacent nucleosome densities, which correspond to the -1 and +1 sequential positions. Each of these adjacent nucleosomes would be connected via short linker DNAs to another nucleosome, corresponding to -2 and +2 positions relative to the middle nucleosome. This line of

282 reasoning fails for nucleosome-depleted positions, but these are in the minority. This
283 linker-DNA imposed close packing supports our model that nucleosomes form small
284 clusters and possibly small chains.

285 Our 2-D and 3-D classification analyses suggest that chromatin structure is
286 irregular from the level of individual nucleosomes to mitotic chromosomes. Unlike the
287 crystal structure (Luger et al., 1997), nucleosomes *in vivo* are largely conformationally
288 heterogeneous. This heterogeneity may arise from interactions with small proteins,
289 assembly/disassembly intermediates, partial unwrapping, or a combination of all these
290 factors. Out of these possibilities, the partial unwrapping of *S. pombe* nucleosomes *in*
291 *vivo* was predicted nearly a decade ago (Zlatanova et al., 2009). This variability in
292 nucleosome structure and linker DNA length can then give rise to irregular
293 oligonucleosome folding (Wong et al., 2007; Collepardo-Guevara and Schlick, 2014).
294 Furthermore, the rarity of face-to-face nucleosome packing precludes chromatin-fiber
295 interdigitation by nucleosome stacking as a major folding motif. Irregular chromatin is
296 therefore a conserved feature in single-celled eukaryotes (Gan et al., 2013; Chen et al.,
297 2016). A recent study using a new DNA negative-staining method concluded that
298 chromatin structure is also irregular in mammalian cells (Ou et al., 2017), which is
299 consistent with earlier EM studies of other mammalian cells (McDowall et al., 1986;
300 Eltsov et al., 2008; Fussner et al., 2012; Nishino et al., 2012).
301

302 **Cryo-ET, Hi-C, and live-cell imaging paint a complex picture of chromatin**
303 Hi-C is a “proximity-based” method wherein two DNA segments can be detected if they
304 are close enough to chemically cross-link (Lieberman-Aiden et al., 2009). In this

interpretation, Hi-C indirectly probes chromatin structure, and is revealing new principles of chromatin organization in *S. pombe* (Mizuguchi et al., 2014; Kakui et al., 2017; Tanizawa et al., 2017). A common Hi-C structural feature is the domain (also called TADs), a contiguous sequence in which nucleosomes are more likely to interact with other nucleosomes within this sequence than outside. *S. pombe* domains range from 40kb to 1Mb long, corresponding to 300 - 7,000 sequential nucleosomes. If domains are monolithic globular bodies as universally depicted in the literature, they should be visible in our cryotomograms as large, densely packed nucleosomes clusters. Such a cluster would be 7 - 20 nucleosomes wide, assuming a simple cuboid shape; other globular shapes would be equally large. The nucleosome clusters we saw were generally much smaller. We propose that small nucleosome clusters, which we see at the single-cell level by cryo-ET, correspond to different loci in each cell. If these clusters belong to Hi-C domains, they would sum to the much-larger structure due the effects of population averaging. As the simplest example, we illustrate how four sequential nucleosomes could give rise to a Hi-C structure that is larger than what can be found in individual cells (Fig. S13). Cell-to-cell variation may also explain differences between single-cell and population-based Hi-C studies (Nagano et al., 2013; Flyamer et al., 2017; Nagano et al., 2017; Stevens et al., 2017).

Two recent studies unexpectedly reported that short-range Hi-C contacts are less probable in mitotic *S. pombe* cells than in interphase cells (Kakui et al., 2017; Tanizawa et al., 2017), echoing a previous study of mitotic human cells (Naumova et al., 2013). Interestingly, quiescent B cells, which have condensed chromosomes, have lower short-range Hi-C contact probabilities than active B cells, which have decondensed

chromosomes (Kieffer-Kwon et al., 2017). If Hi-C detections arise solely from nucleosome-nucleosome proximity, then the nucleosomes should move further apart in mitosis; we observed the opposite. What else, then, could explain the lower short-range Hi-C contact frequency in mitotic cells? A recent study found that within compact (160 nm) mammalian chromatin domains, all nucleosome motion is correlated (Nozaki et al., 2017). We propose that short-range Hi-C contacts in *S. pombe* and some mammalian cells is also dependent on chromatin dynamics (Hihara et al., 2012; Kakui et al., 2017). These dynamics slow down in mitotic cells due to the increase in nucleosome cluster size, and lowers the frequency that crosslinkable groups can interact with each other.

The role of uneven condensation in transcriptional regulation

The strong correlation between mitotic chromosome condensation and transcriptional repression is well established (Taylor, 1960; Prescott and Bender, 1962). Mechanistic evidence of mitotic repression came from the observation that mitotic condensation is coincident with transcription-factor displacement (Martinez-Balbas et al., 1995). Yet, even though transcription is largely downregulated in mitotic *S. pombe* cells, (Oliva et al.), many cell-cycle-regulated genes actually get expressed more (Rustici et al.; Oliva et al.; Peng et al.). In agreement, our immunofluorescence experiments detected elongating RNA polymerase II in mitotic *S. pombe* chromosomes. We propose that chromatin structure at multiple size scales permits access to regulatory sequences, somewhat independently of dynamics. At the mononucleosome level, many chromatin-regulatory complexes recognize and bind to the nucleosome's face (McGinty and Tan, 2015). Because face-to-face nucleosome stacking is exceptionally rare in mitotic cells,

this critical surface remains available for interactions. At the level of the chromosome, fewer megacomplexes are interspersed within the densely packed nucleosomes. However, uneven condensation leaves nucleosome-free positions that could remain permissive to the occasional passage or assembly of megacomplexes such as spliceosomes and transcription preinitiation complexes. If uneven chromosome condensation is highly conserved, the mechanisms proposed here could explain the recent observations of chromatin accessibility and transcription in mitotic mammalian cells (Hsiung et al., 2015; Teves et al., 2016; Palozola et al., 2017).

359 **MATERIALS AND METHODS**

360

361 **Cell culture**

362 *S. pombe* cell culture (Forsburg, 2003), G2-phase arrest (Ducommun et al.) and
363 prometaphase arrest (Hiraoka et al.) were performed as previously reported. *nda3-*
364 *KM311* cells were grown overnight in yeast-extract supplemented (YES) medium (30
365 g/L glucose, 5 g/L yeast extract, 225 mg/L adenine, 225 mg/L histidine, 225 mg/L
366 leucine, 225 mg/L uracil) at 30°C with shaking. When the optical density at 600 nm
367 (OD_{600}) reached ~ 0.2, the cultures were cooled by incubation in a 20°C shaker. After a
368 10-hr incubation at this lower temperature, more than 90% of cells were arrested in
369 prometaphase. *cdc25-22* cells were grown in YES medium at 25°C with shaking
370 overnight. When the OD_{600} reached ~ 0.2, the cultures were warmed to 36°C in a water
371 bath and then transferred to a 36°C shaker. After 4 hr, the majority of cells were
372 arrested at G2 phase. *S. japonicus* cells were grown in YES medium at 30°C with
373 shaking overnight until mid-log phase (OD_{600} ~ 0.6) (Yam et al.).

374

375 **Fluorescence microscopy**

376 Cells were stained with 4',6-diamidino-2-phenylindole (DAPI) following a published
377 protocol (Toda et al.). Cells (1 ml) were fixed with 2.5% formaldehyde for 60 min at the
378 restrictive temperature for mutants. The cells were washed twice by centrifugation at
379 1500 *x g* for 1 min and resuspension with distilled water. They were pelleted at 1500 *x g*
380 for 1 min and stained by resuspension in 50 µl PBS, pH 7.4, containing 1 µg/ml DAPI.
381 Ten µl of the sample was then added to a glass slide and imaged using a PerkinElmer

Ultraview Vox Spinning Disc confocal microscope (PerkinElmer, Waltham, MA). Images were recorded using a 100x oil-immersion objective.

Immunofluorescence

Log-phase cells (10 ml) were fixed with 3.7% formaldehyde for 90 min at 30°C (or at the restrictive temperature for arrested mutants). Cells were then pelleted by centrifugation at 1500 *x g* for 5 min. Cells were then resuspended in 1 ml PEM buffer (0.1 M PIPES pH 6.95, 2 mM EGTA, 1 mM $MgSO_4$). Cells were washed once with 1 ml PEM this way and then resuspended in 1 ml PEMS (1.2 M sorbitol in PEM). Next, cells were spheroplasted for 15 minutes by incubation with lysis-enzyme cocktail (Abcam, cat# ab206997), diluted 1:1000 in PEMS at 30°C. Cells were washed with PEMS. The pellet was then resuspended in PEMS with 1% Triton X-100 and incubated at 22°C for 5 min. Cells were then washed twice with PEM and incubated in PEMBAL (PEM, 1% BSA, 100 mM L-Lysine hydrochloride) at 22°C for 1 hour. Cells were then incubated with rabbit anti-RNA polymerase II CTD-repeat YSPTSPS (phospho S2) antibody in PEMBAL (1:1000 dilution) at 22°C for 1 hour. Cells were washed three times with 1 ml PEMBAL and then incubated with Alexa Fluor 488-coupled donkey anti-rabbit antibodies at 22°C for 1 hour. Cells were then washed three times with PEM and resuspended in 50 µl of 1 µg/ml DAPI.

Self-pressurized freezing

Self-pressurized freezing was performed based on a previous method, with modifications (Yakovlev and Downing, 2011). *S. pombe* cells were grown in YES

405 medium until the OD_{600} reached 0.2 - 0.6. Cells were pelleted by centrifuging at 1500 *x*
406 *g* for 5 min. Concentrated dextran stock (40 kDa, 60% w/v, in YES) was added to the
407 cell pellet as an extracellular cryoprotectant to a final concentration of 30%. The cells
408 were then quick-spun to remove air bubbles and then loaded into a copper tube (0.45 /
409 0.3 mm outer / inner diameters) with a syringe-type filler device (Part 733-1,
410 Engineering Office M. Wohlwend GmbH). The tube was sealed by crimping both ends
411 with flat-jaw pliers. The sealed tube was held horizontally, ~ 3 cm above the liquid-
412 ethane cryogen surface, and then dropped in. The flattened ends of the tube were then
413 removed with a tube-cutting device under liquid nitrogen.
414
415 **Vitreous sectioning**
416 Vitreous sectioning was performed as previously described with modifications (Chen et
417 al., 2016). A perforated- or continuous-carbon grid was coated with 10-nm gold colloids
418 as fiducials for cryotomographic alignment. Gold solution (5 µl at 5.7 x 10^{12} particles/ml)
419 in 0.1 mg/ml BSA was applied to the grid and then air-dried. Frozen-hydrated cells were
420 cut into a 70-nm-thick frozen-hydrated ribbon using a 35° diamond knife (Cryo35,
421 Diatome, Nidau, Switzerland) in a Leica UC7/FC7 cryo-ultramicrotome (Leica
422 Microsystems, Vienna, Austria) at -150°C. Once the ribbon was ~ 3 mm long, the
423 colloidal-gold-coated EM grid was placed underneath the ribbon. To minimize occlusion
424 by grid bars at high tilt during cryotomographic imaging, the grid as aligned so that the
425 ribbon was in between and parallel with the grid bars. The ribbon was then attached to
426 the grid by operating the Crion in “charge” mode for ~ 30 seconds. The grid was stored
427 in liquid nitrogen until imaging.

428

429 **Cell lysis**

430 Log-phase *S. pombe* cells were pelleted by centrifuging at 1500 *x g* for 5 min and then
431 spheroplasted for 15 minutes by incubation with lysis-enzyme cocktail at either 30°C or
432 at the restrictive temperature for mutants. The spheroplasts were pelleted at 1500 *x g*
433 for 2 min at 22°C and then lysed in 20 µl lysis buffer (50 mM EDTA and a 1:1000
434 dilution of protease inhibitor cocktail, Abcam, cat# ab206997) on ice for 15 min.

435

436 **Plunge freezing**

437 Plunge freezing was done using a Vitrobot Mk IV (Thermo, Waltham, MA) operated at
438 4°C with 80% humidity. *S. pombe* cell lysates (4 µl) were applied to a freshly glow-
439 discharged perforated-carbon grid. The grid was blotted once (blot force: 1, blot time: 3
440 seconds) with filter paper (Whatman #1001055) and then plunged into liquid ethane.

441

442 **Cryo-electron tomography**

443 Tilt series were collected using FEI TOMO4 on a Titan Krios cryo-TEM (Thermo,
444 Waltham, MA) operated at 300 KeV and equipped with a field-emission gun, a Volta
445 phase-plate device, and a Falcon II direct-detection camera. Details of the imaging
446 parameters are shown in Table S1. Image alignment, CTF compensation, low-pass
447 filtering, and 3-D reconstruction were all done using the IMOD software package
448 (Kremer et al., 1996; Mastronarde, 1997; Xiong et al., 2009). Note that Volta
449 cryotomograms were not CTF compensated. Cryotomograms were visualized as

450 tomographic slices with 3dmod and as isosurfaces with UCSF Chimera (Pettersen et
451 al., 2004).
452
453 **Template matching**
454 Template matching was done using PEET (Heumann, 2016). A manually-selected
455 subtomogram containing a nucleosome-like particle served as a template. The influence
456 of the surrounding nucleoplasmic densities were suppressed by the application of a
457 spherical mask. A search was performed on a grid with a 10-nm spacing within the
458 nucleus. Template-matching hits within 6 nm were considered as duplicates and the
459 extra hit was automatically removed. The cross-correlation coefficient cutoff criteria
460 were the same as in our previous report (Cai et al., 2017). Briefly, the average cross-
461 correlation coefficients of all template-matching hits was used as an initial cutoff. This
462 cutoff was then manually adjusted (if needed) to minimize the number of detectable
463 false positives and false negatives. To further remove false positives from
464 megacomplexes, another round of template matching was performed using a ribosome-
465 like density selected within the tomogram as a template. The nucleosome hits that were
466 within 12.5 nm of these megacomplexes were then removed with a Matlab script
467 (available on request; Mathworks, Natick, MA).
468 For dinucleosome template matching, a manually-selected subtomogram of a di-
469 nucleosome served as a template. A cylindrical mask (15-nm diameter, 22-nm height),
470 rotated to align with the long axis of the dinucleosome template, was used to suppress
471 the background surrounding densities. The search grid with a 25-nm spacing was
472 generated within the nucleus. Owing to the missing-wedge artifact, nucleosomes have

higher resolution in the X-Y plane. Therefore, the angular search was limited only to the Z axis. Hits within 15 nm were considered as duplicates. The cross-correlation coefficient cutoff criteria were the same as described above for mononucleosomes. False positives from megacomplexes fell into their own classes in the subsequent 2-D classification run (see below) and were removed.

Reference-free 2-D and 3-D classification

Subtomogram classification and 3-D averaging of nucleosomes were done in RELION 1.4 and RELION 2.0 (Scheres, 2012a, b; Bharat et al., 2015; Kimanius et al., 2016), following the workflow of our previous study (Cai et al., 2017). The template-matching hit coordinates were imported into RELION and then particles were extracted with a 15.6-nm box and masked with a 13.5-nm-diameter sphere. For 2-D classification, the number of classes was set to 50 and the resolution of was limited to 3 nm. All nucleosome-like classes were selected. For 3-D classification, the number of classes was set to between 10 and 20, and the resolution was limited to 2-3 nm. Two to three rounds of 3-D classification were performed. False-positive were manually removed in between rounds.

For di-nucleosome 2-D classification, the box size and the mask diameter were set to 30 nm and 26 nm, respectively. As a default setting, RELION produces projections of all densities within the boxes, including the nucleoplasmic densities above and below dinucleosomes. To include only the dinucleosome densities, a python script (available on request) was used to generate projections from a 17.5-nm thick tomographic slice. The resolution of the data was limited to 2 nm to suppress the effects

of high-resolution noise. The number of classes was set to 100, but many of the classes were very similar and therefore merged.

Nearest-neighbor distance analysis

Nearest-neighbor distance analysis of template-matching hits (Figs. 5 and S9) was performed as previously described (Cai et al., 2017). The coordinates of the nucleosome hits were imported into Matlab. NND and 10^{th} NND were calculated using the Matlab function nearestneighbour.m (custom script available on request).

Statistical analysis

Two-tailed t-tests for NND values were performed in Excel using the TTEST function. The number of NND values analysed for G2-phase and prometaphase *S. pombe*, interphase and mitotic *S. japonicus* were 10292, 11835, 9397, 4474, respectively.

Data sharing

A cryotomogram, corresponding to Fig. 4, was deposited in the EMDataBank as EMD-6846. The tilt series for all cryotomograms presented in this manuscript were deposited in the Electron Microscopy Public Image Archive as EMPIAR-10125.

Acknowledgements

We thank the CBIS microscopy staff for support and training. We thank Snezhka Oliferenko for advice on *S. japonicus* culture and manuscript feedback; Mohan Balasubramanian for feedback and sharing *S. pombe* strains; Kazuhiro Maeshima for

519 feedback. *S. japonicus* strains were obtained from JapoNet. SC, CC, ZT and LG were
520 supported by NUS startups R-154-000-515-133, R-154-000-524-651, and D-E12-303-
521 154-217, R-154-000-558-133, and MOE T2 R-154-000-624-112.

522

523 **Contributions**

524 S.C - experiments, project design, writing, CC - training, YH - training, ZYT -
525 experiments, JS - training, LG - project design, writing.

526

References

Allen, B.L., and Taatjes, D.J. (2015). The Mediator complex: a central integrator of transcription. Nature reviews Molecular cell biology *16*, 155-166.

Beliveau, B.J., Boettiger, A.N., Avendano, M.S., Jungmann, R., McCole, R.B., Joyce, E.F., Kim-Kiselak, C., Bantignies, F., Fonseka, C.Y., Erceg, J.*, et al.* (2015). Single-molecule super-resolution imaging of chromosomes and in situ haplotype visualization using Oligopaint FISH probes. Nature communications *6*, 7147.

Ben-Shem, A., Garreau de Loubresse, N., Melnikov, S., Jenner, L., Yusupova, G., and Yusupov, M. (2011). The structure of the eukaryotic ribosome at 3.0 A resolution. Science *334*, 1524-1529.

Bharat, T.A., Russo, C.J., Lowe, J., Passmore, L.A., and Scheres, S.H. (2015). Advances in Single-Particle Electron Cryomicroscopy Structure Determination applied to Sub-tomogram Averaging. Structure *23*, 1743-1753.

Bharat, T.A., and Scheres, S.H. (2016). Resolving macromolecular structures from electron cryo-tomography data using subtomogram averaging in RELION. Nat Protoc *11*, 2054-2065.

Cai, S., Song, Y., Chen, C., Shi, J., and Gan, L. (2017). Natural Chromatin Is Heterogeneous And Self Associates In Vitro. bioRxiv, 139543.

Chen, C., Lim, H.H., Shi, J., Tamura, S., Maeshima, K., Surana, U., and Gan, L. (2016). Budding yeast chromatin is dispersed in a crowded nucleoplasm in vivo. Molecular biology of the cell *27*, 3357-3368.

Collepardo-Guevara, R., and Schlick, T. (2014). Chromatin fiber polymorphism triggered by variations of DNA linker lengths. Proceedings of the National Academy of Sciences of the United States of America *111*, 8061-8066.

Dixon, J.R., Gorkin, D.U., and Ren, B. (2016). Chromatin Domains: The Unit of Chromosome Organization. Molecular cell *62*, 668-680.

553 Dixon, J.R., Selvaraj, S., Yue, F., Kim, A., Li, Y., Shen, Y., Hu, M., Liu, J.S., and Ren, B.
554 (2012). Topological domains in mammalian genomes identified by analysis of chromatin
555 interactions. Nature *485*, 376-380.

556 Ducommun, B., Draetta, G., Young, P., and Beach, D. (1990). Fission yeast cdc25 is a
557 cell-cycle regulated protein. Biochemical and biophysical research communications *167*,
558 301-309.

559 Ekundayo, B., Richmond, T.J., and Schalch, T. (2017). Capturing Structural
560 Heterogeneity in Chromatin Fibers. Journal of molecular biology *429*, 3031-3042.

561 Eltsov, M., Maclellan, K.M., Maeshima, K., Frangakis, A.S., and Dubochet, J. (2008).
562 Analysis of cryo-electron microscopy images does not support the existence of 30-nm
563 chromatin fibers in mitotic chromosomes in situ. Proceedings of the National Academy
564 of Sciences of the United States of America *105*, 19732-19737.

565 Engel, B.D., Schaffer, M., Kuhn Cuellar, L., Villa, E., Plitzko, J.M., and Baumeister, W.
566 (2015). Native architecture of the Chlamydomonas chloroplast revealed by in situ cryo-
567 electron tomography. Elife *4*.

568 Fantes, P. (1979). Epistatic gene interactions in the control of division in fission yeast.
569 Nature *279*, 428-430.

570 Fei, J., Torigoe, S.E., Brown, C.R., Khuong, M.T., Kassavetis, G.A., Boeger, H., and
571 Kadonaga, J.T. (2015). The prenucleosome, a stable conformational isomer of the
572 nucleosome. Genes & development *29*, 2563-2575.

573 Flyamer, I.M., Gassler, J., Imakaev, M., Brandao, H.B., Ulianov, S.V., Abdennur, N.,
574 Razin, S.V., Mirny, L.A., and Tachibana-Konwalski, K. (2017). Single-nucleus Hi-C
575 reveals unique chromatin reorganization at oocyte-to-zygote transition. Nature *544*, 110-
576 114.

577 Forsburg, S.L. (2003). Growth and manipulation of S. pombe. Current Protocols in
578 Molecular Biology, 13.16. 11-13.16. 17.

579 Fussner, E., Strauss, M., Djuric, U., Li, R., Ahmed, K., Hart, M., Ellis, J., and Bazett-
580 Jones, D.P. (2012). Open and closed domains in the mouse genome are configured as
581 10-nm chromatin fibres. EMBO Rep *13*, 992-996.

582 Gan, L., and Jensen, G.J. (2012). Electron tomography of cells. Quarterly reviews of
583 biophysics *45*, 27-56.

584 Gan, L., Ladinsky, M.S., and Jensen, G.J. (2013). Chromatin in a marine picoeukaryote
585 is a disordered assemblage of nucleosomes. Chromosoma *122*, 377-386.

586 Gleizes, P.E., Noaillac-Depeyre, J., Leger-Silvestre, I., Teulieres, F., Dauxois, J.Y.,
587 Pommet, D., Azum-Gelade, M.C., and Gas, N. (2001). Ultrastructural localization of
588 rRNA shows defective nuclear export of preribosomes in mutants of the Nup82p
589 complex. The Journal of cell biology *155*, 923-936.

590 Harlen, K.M., and Churchman, L.S. (2017). The code and beyond: transcription
591 regulation by the RNA polymerase II carboxy-terminal domain. Nature reviews
592 Molecular cell biology *18*, 263-273.

593 Heumann, J.M. (2016). PEET (University of Colorado Boulder).

594 Hihara, S., Pack, C.G., Kaizu, K., Tani, T., Hanafusa, T., Nozaki, T., Takemoto, S.,
595 Yoshimi, T., Yokota, H., Imamoto, N.*, et al.* (2012). Local nucleosome dynamics
596 facilitate chromatin accessibility in living mammalian cells. Cell reports *2*, 1645-1656.

597 Hirano, T. (2016). Condensin-Based Chromosome Organization from Bacteria to
598 Vertebrates. Cell *164*, 847-857.

599 Hiraoka, Y., Toda, T., and Yanagida, M. (1984). The NDA3 gene of fission yeast
600 encodes beta-tubulin: a cold-sensitive nda3 mutation reversibly blocks spindle formation
601 and chromosome movement in mitosis. Cell *39*, 349-358.

602 Hsiung, C.C., Morrissey, C.S., Udugama, M., Frank, C.L., Keller, C.A., Baek, S.,
603 Giardine, B., Crawford, G.E., Sung, M.H., Hardison, R.C.*, et al.* (2015). Genome

604 accessibility is widely preserved and locally modulated during mitosis. Genome Res *25*,
605 213-225.

606 Kakui, Y., Rabinowitz, A., Barry, D.J., and Uhlmann, F. (2017). Condensin-mediated
607 remodeling of the mitotic chromatin landscape in fission yeast. Nat Genet *49*, 1553-
608 1557.

609 Khoshouei, M., Radjainia, M., Baumeister, W., and Danev, R. (2017). Cryo-EM structure
610 of haemoglobin at 3.2 A determined with the Volta phase plate. Nature communications
611 *8*, 16099.

612 Kieffer-Kwon, K.R., Nimura, K., Rao, S.S.P., Xu, J., Jung, S., Pekowska, A., Dose, M.,
613 Stevens, E., Mathe, E., Dong, P.*, et al.* (2017). Myc Regulates Chromatin
614 Decompaction and Nuclear Architecture during B Cell Activation. Molecular cell *67*, 566-
615 578 e510.

616 Kimanius, D., Forsberg, B.O., Scheres, S.H., and Lindahl, E. (2016). Accelerated cryo-
617 EM structure determination with parallelisation using GPUs in RELION-2. Elife *5*.

618 Komarnitsky, P., Cho, E.J., and Buratowski, S. (2000). Different phosphorylated forms
619 of RNA polymerase II and associated mRNA processing factors during transcription.
620 Genes & development *14*, 2452-2460.

621 Kremer, J.R., Mastronarde, D.N., and McIntosh, J.R. (1996). Computer visualization of
622 three-dimensional image data using IMOD. Journal of structural biology *116*, 71-76.

623 Kubik, S., Bruzzone, M.J., Jacquet, P., Falcone, J.L., Rougemont, J., and Shore, D.
624 (2015). Nucleosome Stability Distinguishes Two Different Promoter Types at All Protein-
625 Coding Genes in Yeast. Molecular cell *60*, 422-434.

626 Lantermann, A.B., Straub, T., Stralfors, A., Yuan, G.C., Ekwall, K., and Korber, P.
627 (2010). Schizosaccharomyces pombe genome-wide nucleosome mapping reveals
628 positioning mechanisms distinct from those of Saccharomyces cerevisiae. Nat Struct
629 Mol Biol *17*, 251-257.

630 Lieberman-Aiden, E., van Berkum, N.L., Williams, L., Imakaev, M., Ragoczy, T., Telling,
631 A., Amit, I., Lajoie, B.R., Sabo, P.J., Dorschner, M.O.*, et al.* (2009). Comprehensive
632 mapping of long-range interactions reveals folding principles of the human genome.
633 Science *326*, 289-293.

634 Luger, K., Mader, A.W., Richmond, R.K., Sargent, D.F., and Richmond, T.J. (1997).
635 Crystal structure of the nucleosome core particle at 2.8 A resolution. Nature *389*, 251-
636 260.

637 Maeshima, K., and Eltsov, M. (2008). Packaging the genome: the structure of mitotic
638 chromosomes. J Biochem *143*, 145-153.

639 Martinez-Balbas, M.A., Dey, A., Rabindran, S.K., Ozato, K., and Wu, C. (1995).
640 Displacement of sequence-specific transcription factors from mitotic chromatin. Cell *83*,
641 29-38.

642 Mastronarde, D.N. (1997). Dual-axis tomography: an approach with alignment methods
643 that preserve resolution. Journal of structural biology *120*, 343-352.

644 McDowall, A.W., Smith, J.M., and Dubochet, J. (1986). Cryo-electron microscopy of
645 vitrified chromosomes in situ. EMBO J *5*, 1395-1402.

646 McGinty, R.K., and Tan, S. (2015). Nucleosome structure and function. Chem Rev *115*,
647 2255-2273.

648 Mizuguchi, T., Fudenberg, G., Mehta, S., Belton, J.M., Taneja, N., Folco, H.D.,
649 FitzGerald, P., Dekker, J., Mirny, L., Barrowman, J.*, et al.* (2014). Cohesin-dependent
650 globules and heterochromatin shape 3D genome architecture in S. pombe. Nature *516*,
651 432-435.

652 Nagano, T., Lubling, Y., Stevens, T.J., Schoenfelder, S., Yaffe, E., Dean, W., Laue,
653 E.D., Tanay, A., and Fraser, P. (2013). Single-cell Hi-C reveals cell-to-cell variability in
654 chromosome structure. Nature *502*, 59-64.

Nagano, T., Lubling, Y., Varnai, C., Dudley, C., Leung, W., Baran, Y., Mendelson Cohen, N., Wingett, S., Fraser, P., and Tanay, A. (2017). Cell-cycle dynamics of chromosomal organization at single-cell resolution. Nature *547*, 61-67.

Naumova, N., Imakaev, M., Fudenberg, G., Zhan, Y., Lajoie, B.R., Mirny, L.A., and Dekker, J. (2013). Organization of the mitotic chromosome. Science *342*, 948-953.

Nishino, Y., Eltsov, M., Joti, Y., Ito, K., Takata, H., Takahashi, Y., Hihara, S., Frangakis, A.S., Imamoto, N., Ishikawa, T.*, et al.* (2012). Human mitotic chromosomes consist predominantly of irregularly folded nucleosome fibres without a 30-nm chromatin structure. EMBO J *31*, 1644-1653.

Nozaki, T., Imai, R., Tanbo, M., Nagashima, R., Tamura, S., Tani, T., Joti, Y., Tomita, M., Hibino, K., Kanemaki, M.T.*, et al.* (2017). Dynamic Organization of Chromatin Domains Revealed by Super-Resolution Live-Cell Imaging. Molecular cell *67*, 282-293 e287.

Oesterreich, F.C., Herzel, L., Straube, K., Hujer, K., Howard, J., and Neugebauer, K.M. (2016). Splicing of Nascent RNA Coincides with Intron Exit from RNA Polymerase II. Cell *165*, 372-381.

Oliva, A., Rosebrock, A., Ferrezuelo, F., Pyne, S., Chen, H., Skiena, S., Futcher, B., and Leatherwood, J. (2005). The cell cycle-regulated genes of Schizosaccharomyces pombe. PLoS Biol *3*, e225.

Ou, H.D., Phan, S., Deerinck, T.J., Thor, A., Ellisman, M.H., and O'Shea, C.C. (2017). ChromEMT: Visualizing 3D chromatin structure and compaction in interphase and mitotic cells. Science *357*.

Palozola, K.C., Donahue, G., Liu, H., Grant, G.R., Becker, J.S., Cote, A., Yu, H., Raj, A., and Zaret, K.S. (2017). Mitotic transcription and waves of gene reactivation during mitotic exit. Science *358*, 119-122.

680 Peng, X., Karuturi, R.K., Miller, L.D., Lin, K., Jia, Y., Kondu, P., Wang, L., Wong, L.S.,
681 Liu, E.T., Balasubramanian, M.K.*, et al.* (2005). Identification of cell cycle-regulated
682 genes in fission yeast. Molecular biology of the cell *16*, 1026-1042.

683 Pettersen, E.F., Goddard, T.D., Huang, C.C., Couch, G.S., Greenblatt, D.M., Meng,
684 E.C., and Ferrin, T.E. (2004). UCSF Chimera--a visualization system for exploratory
685 research and analysis. J Comput Chem *25*, 1605-1612.

686 Pombo, A., and Dillon, N. (2015). Three-dimensional genome architecture: players and
687 mechanisms. Nature reviews Molecular cell biology *16*, 245-257.

688 Prescott, D.M., and Bender, M.A. (1962). Synthesis of RNA and protein during mitosis
689 in mammalian tissue culture cells. Exp Cell Res *26*, 260-268.

690 Ricci, M.A., Manzo, C., Garcia-Parajo, M.F., Lakadamyali, M., and Cosma, M.P. (2015).
691 Chromatin fibers are formed by heterogeneous groups of nucleosomes in vivo. Cell *160*,
692 1145-1158.

693 Robinow, C.F., and Hyams, J.S. (1989). General Cytology of Fission Yeasts. In
694 Molecular biology of the fission yeast, A. Nasim, P. Young, and B.F. Johnson, eds. (San
695 Diego: Academic Press), pp. 273-330.

696 Rustici, G., Mata, J., Kivinen, K., Lio, P., Penkett, C.J., Burns, G., Hayles, J., Brazma,
697 A., Nurse, P., and Bahler, J. (2004). Periodic gene expression program of the fission
698 yeast cell cycle. Nat Genet *36*, 809-817.

699 Scheres, S.H. (2012a). A Bayesian view on cryo-EM structure determination. Journal of
700 molecular biology *415*, 406-418.

701 Scheres, S.H. (2012b). RELION: implementation of a Bayesian approach to cryo-EM
702 structure determination. Journal of structural biology *180*, 519-530.

703 Stevens, T.J., Lando, D., Basu, S., Atkinson, L.P., Cao, Y., Lee, S.F., Leeb, M.,
704 Wohlfahrt, K.J., Boucher, W., O'Shaughnessy-Kirwan, A.*, et al.* (2017). 3D structures of
705 individual mammalian genomes studied by single-cell Hi-C. Nature *544*, 59-64.

706 Struhl, K. (1998). Histone acetylation and transcriptional regulatory mechanisms. Genes
707 & development *12*, 599-606.

708 Tanizawa, H., Kim, K.D., Iwasaki, O., and Noma, K.I. (2017). Architectural alterations of
709 the fission yeast genome during the cell cycle. Nat Struct Mol Biol.

710 Taylor, J.H. (1960). Nucleic acid synthesis in relation to the cell division cycle. Ann N Y
711 Acad Sci *90*, 409-421.

712 Teves, S.S., An, L., Hansen, A.S., Xie, L., Darzacq, X., and Tjian, R. (2016). A dynamic
713 mode of mitotic bookmarking by transcription factors. Elife *5*.

714 Toda, T., Yamamoto, M., and Yanagida, M. (1981). Sequential alterations in the nuclear
715 chromatin region during mitosis of the fission yeast Schizosaccharomyces pombe: video
716 fluorescence microscopy of synchronously growing wild-type and cold-sensitive cdc
717 mutants by using a DNA-binding fluorescent probe. J Cell Sci *52*, 271-287.

718 White, C.L., Suto, R.K., and Luger, K. (2001). Structure of the yeast nucleosome core
719 particle reveals fundamental changes in internucleosome interactions. EMBO J *20*,
720 5207-5218.

721 Wong, H., Victor, J.M., and Mozziconacci, J. (2007). An all-atom model of the chromatin
722 fiber containing linker histones reveals a versatile structure tuned by the nucleosomal
723 repeat length. PloS one *2*, e877.

724 Xiong, Q., Morphew, M.K., Schwartz, C.L., Hoenger, A.H., and Mastronarde, D.N.
725 (2009). CTF determination and correction for low dose tomographic tilt series. Journal of
726 structural biology *168*, 378-387.

727 Yakovlev, S., and Downing, K.H. (2011). Freezing in sealed capillaries for preparation of
728 frozen hydratedsections. J Microsc *244*, 235-247.

729 Yam, C., Gu, Y., and Oliferenko, S. (2013). Partitioning and remodeling of the
730 Schizosaccharomyces japonicus mitotic nucleus require chromosome tethers. Current
731 biology : CB *23*, 2303-2310.

732 Zlatanova, J., Bishop, T.C., Victor, J.M., Jackson, V., and van Holde, K. (2009). The
733 nucleosome family: dynamic and growing. Structure *17*, 160-171.
734

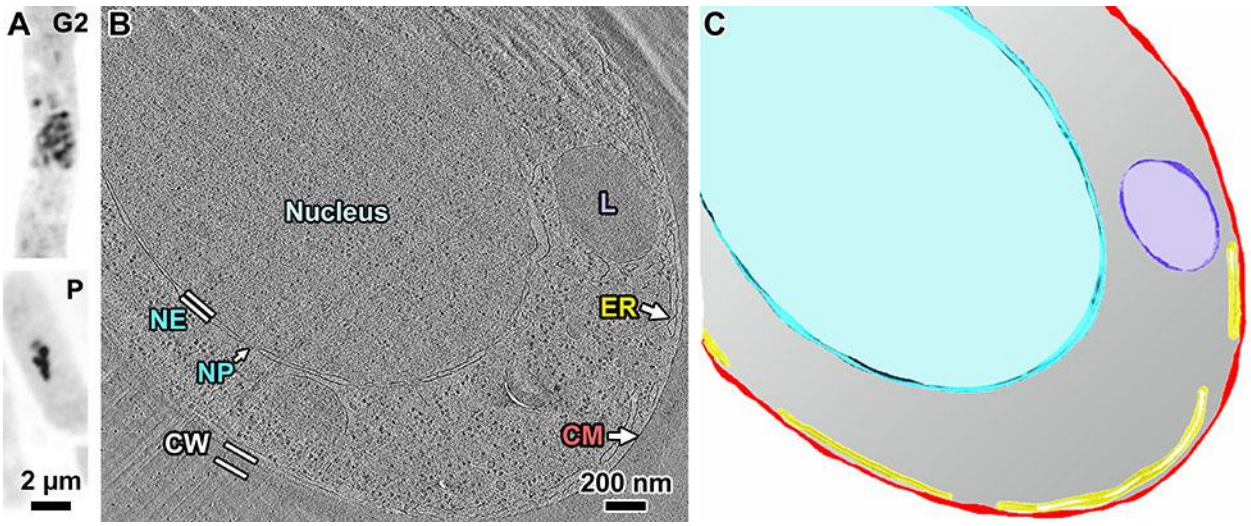

Figure 1. Strategy to study chromosome condensation in *S. pombe*.

(A) Fluorescence images of DAPI-stained G2-phase and prometaphase (P) cells, with contrast inverted for clarity. (B) Cryotomographic slice (25 nm) of a G2-phase cell. NE: nuclear envelope; NP: nuclear pore; L: lipid body; ER: endoplasmic reticulum; CM: cell membrane; CW: cell wall. The wavy features in the upper portion of the cryotomogram are crevasses from sectioning; the thin parallel lines running from 2 to 8 O'clock are knife marks. (C) Segmentation of the cryotomographic slice in panel B, showing the cytological features with the same color scheme as the text labels from panel A.

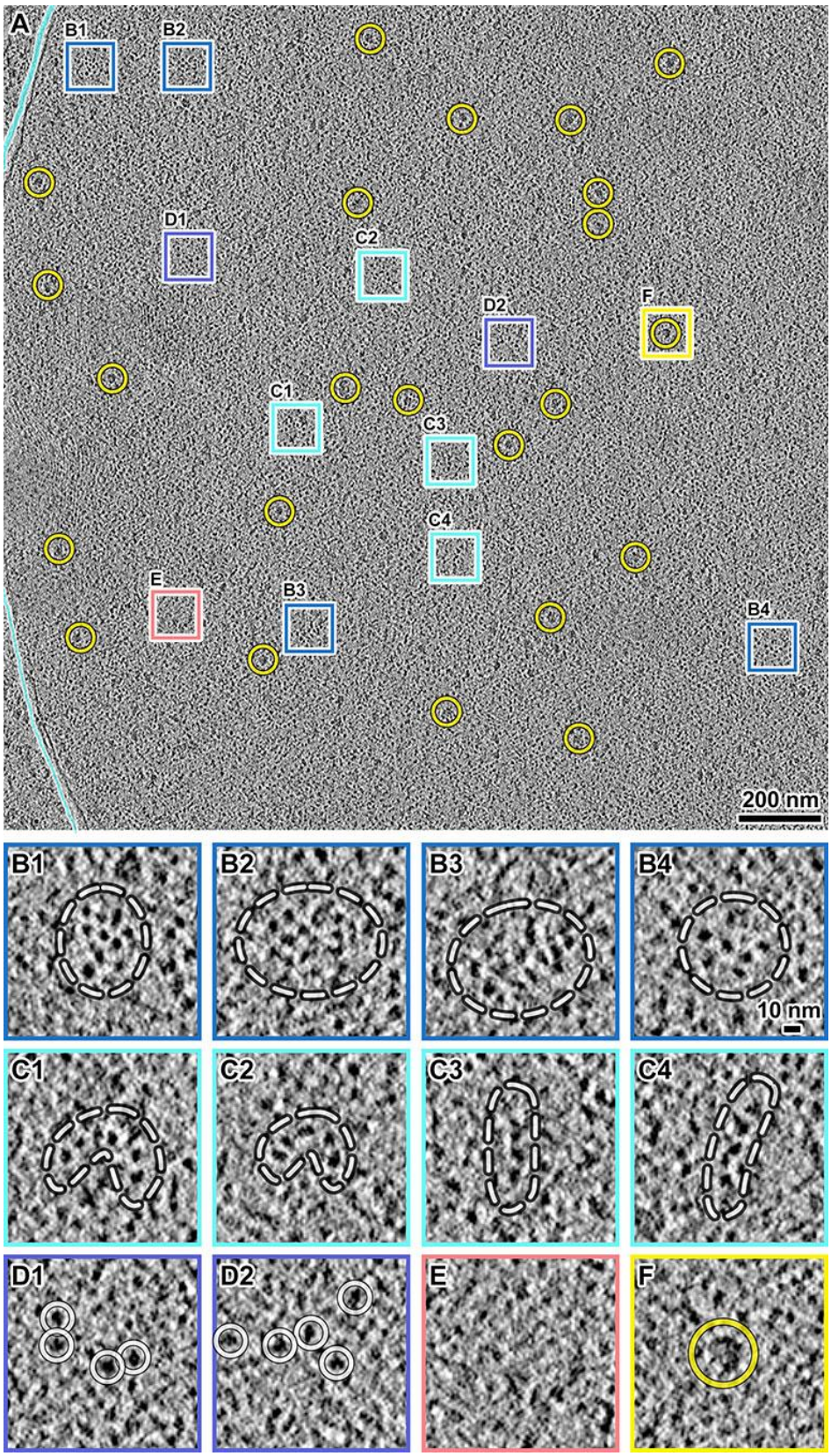

744

Figure 2. *S. pombe* G2-phase chromatin consists of irregularly packed nucleosomes and dispersed megacomplexes.

(A) Cryotomographic slice (10 nm) of an interphase nucleus. Yellow circles: a subset of megacomplexes. The cyan lines denote the nuclear envelope. (B1 - B4) Four examples of nucleosome clusters. (C1 - C4) Four examples of nucleosome chains. In panels B and C, the white dashed lines delineate the approximate boundaries of the nucleosome clusters. Owing to the close packing and particulate nature of nucleosomes, it is not possible to annotate the exact “outline” of a nucleosome cluster. It is also not possible to determine how the nucleosomes are connected by linker DNAs, which generally cannot be seen. (D1 - D2) Two examples of loosely packed nucleosomes, which are circled. (E) An example position that has few nucleosomes. (F) An example megacomplex (circled).

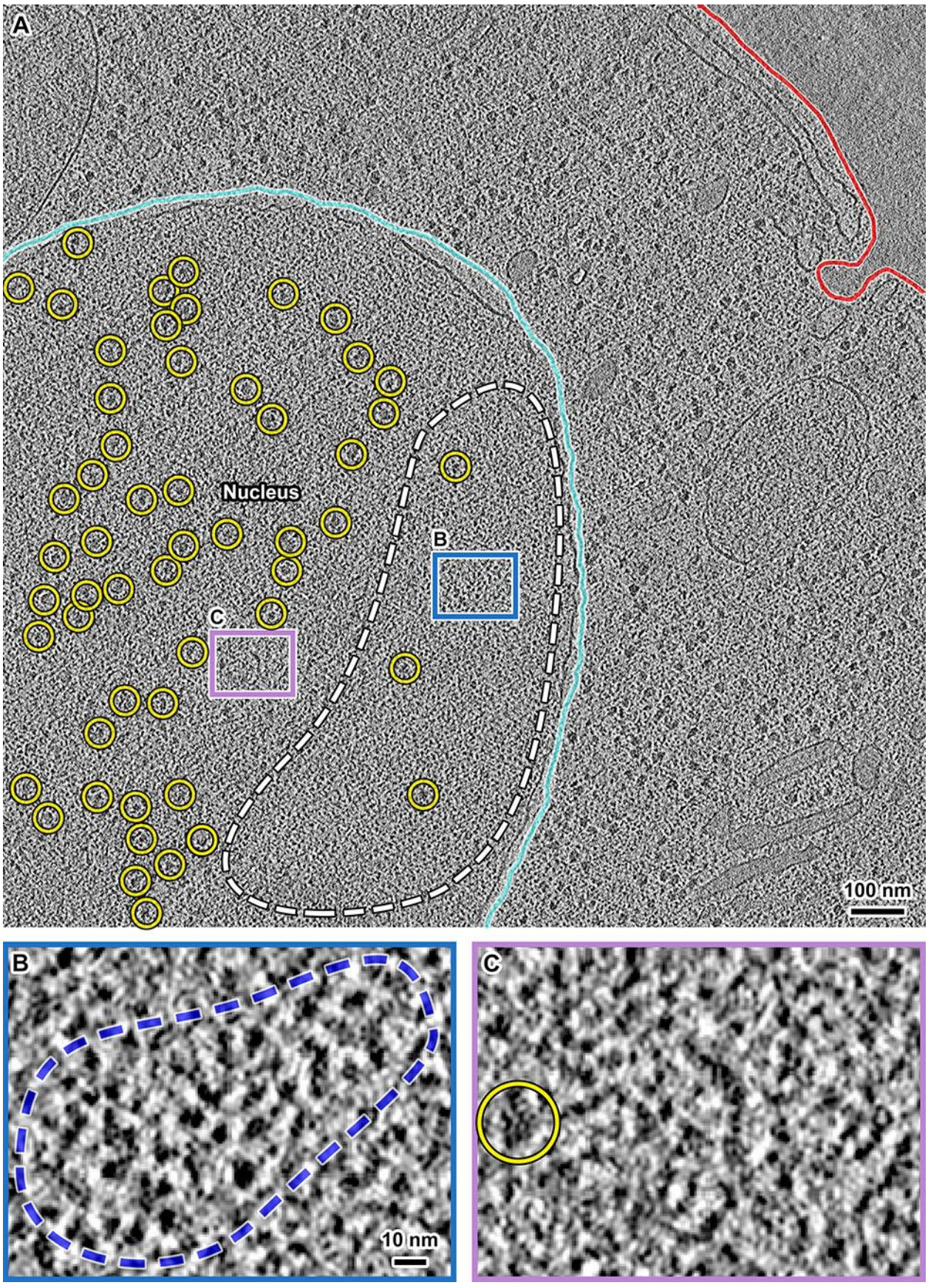

757

Figure 3. Condensed *S. pombe* mitotic chromosomes contain few megacomplexes.

(A) Cryotomographic slice (11 nm) of a prometaphase cell. Cyan line: nuclear envelope, red line: plasma membrane, yellow circles: megacomplexes. The position circled with the dashed white line is a condensed chromosome. Rectangular boxes are enlarged 6-fold in panels B and C. (B) An example position with many nucleosome-like densities forming a cluster, circled with a dashed blue line. (C) An example position without nucleosome-like densities. Yellow circle: a megacomplex.

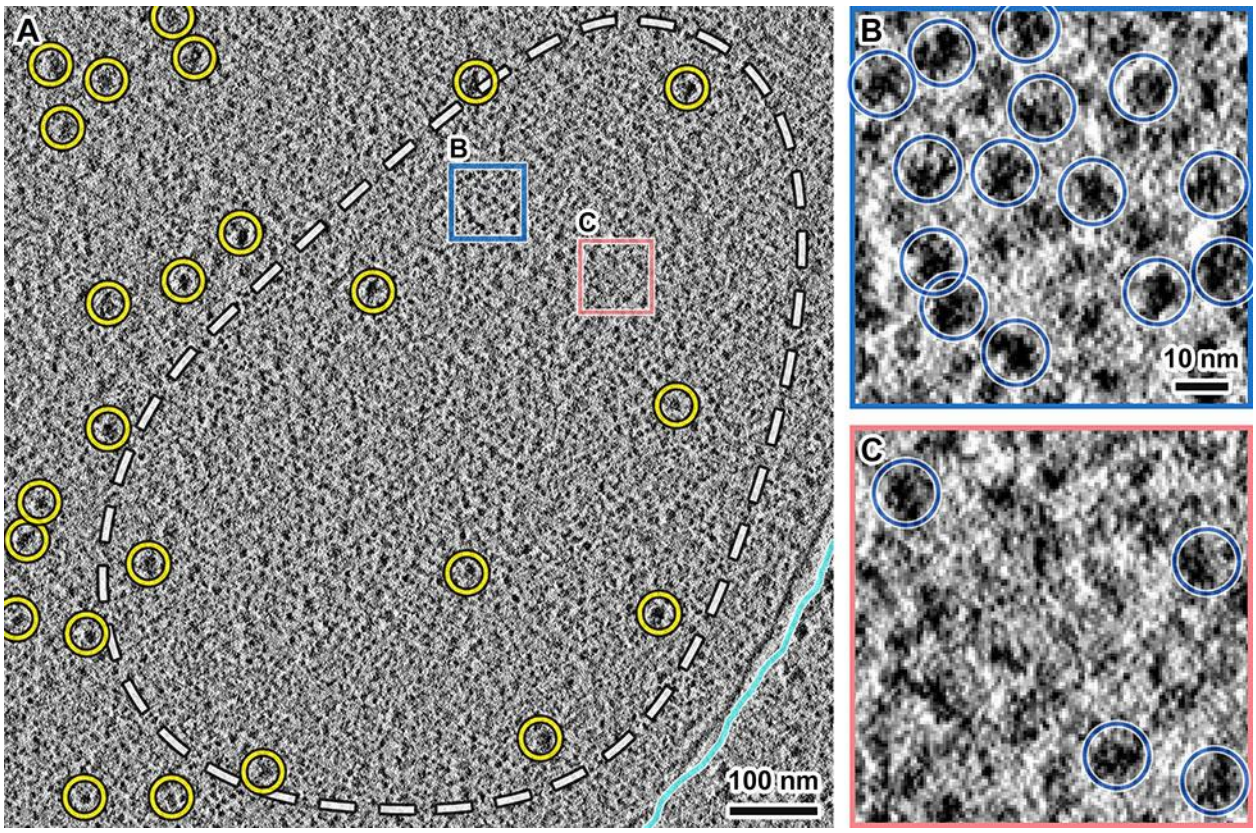

Figure 4: Larger nucleosome clusters and loosely packed nucleosomes coexist within *S. pombe* mitotic condensed chromosomes.

(A) Cryotomographic slice (11 nm) of a nucleus in a prometaphase cell, imaged with Volta phase contrast. White dashed line: approximate chromosome boundary. Yellow circles: megacomplexes. The positions in the blue and salmon boxes are enlarged six-fold in panels B and C, respectively. (B) A position within the mitotic chromosome that contains many closely packed nucleosomes. (C) A position within the mitotic chromosome that contains fewer, loosely packed nucleosomes. Blue circles: nucleosomes.

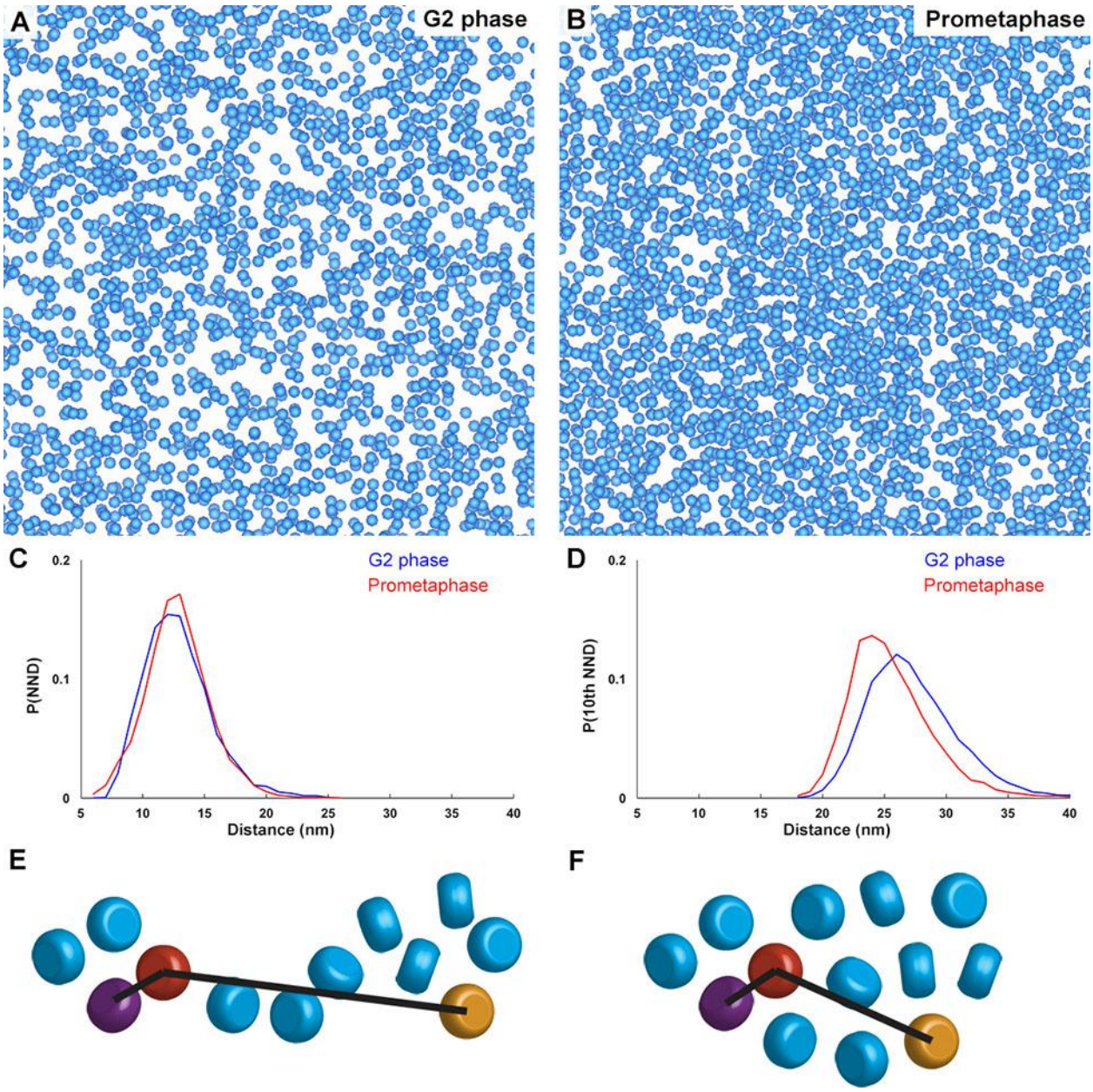

776

777

778 **Figure 5: *S. pombe* nucleosome clusters are larger in prometaphase but have the**

779 **same local packing density.**

780 (A and B) Template-matching hits of nucleosome positions (blue spheres) in Volta

781 cryotomograms of a G2-phase (A) and a prometaphase (B) cell. (C) Nearest-neighbor

782 distance (NND) analysis of template-matching hits. X-axis: NND, 1-nm bins, Y-axis:

783 normalized probability. (D) Tenth NND analysis of template-matching hits. The X- and
784 Y- axes are the same as in panel C. (E and F) Cartoons showing how a small (E) and a
785 large cluster (F) of nucleosomes (rounded cylinders) could have the same NND, but
786 different 10^{th} NND. In each panel, the purple and orange nucleosomes are the
787 respective nearest and 10^{th}-nearest neighbors of the red nucleosome. These cartoons
788 do not show linker DNA, most of which cannot be seen in the Volta cryotomograms.

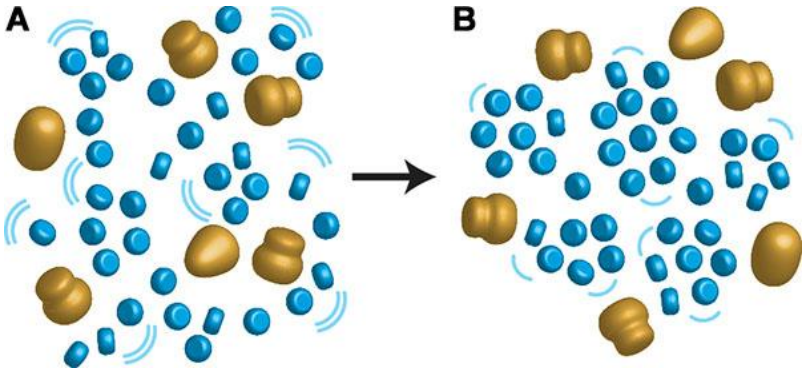

Figure 6: Mitotic chromatin is slightly more compact and less dynamic.

(A) Interphase chromatin consists of both small nucleosome clusters and loosely packed nucleosomes. Blue pills: nucleosome; large gold bodies: megacomplexes. Megacomplexes (pre-ribosomes, spliceosomes, transcription preinitiation complexes) are interspersed between the nucleosomes and nucleosome-free pockets. (B) In condensed mitotic chromosomes, most nucleosomes form large clusters, thereby excluding or inhibiting the assembly of megacomplexes. Furthermore, chromatin dynamics (magnitude proportional to the size and number of the curved lines) also decrease. In both interphase and mitotic chromatin, ordered motifs such as face-to-face nucleosome-nucleosome interactions are largely absent.

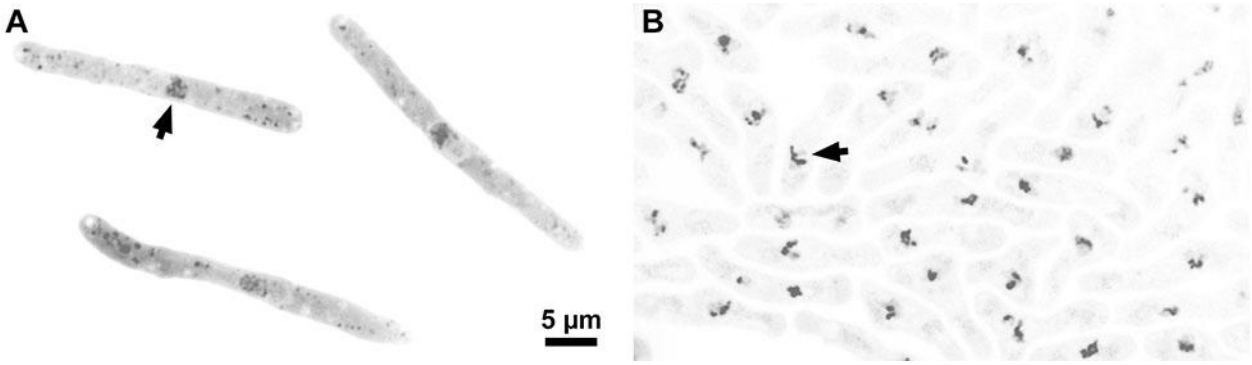

Figure S1: Synchronisation of *S. pombe*.

(A and B) Fluorescence micrographs of DAPI-stained G2-phase (A) and prometaphase (B) cells. The contrast is inverted for clarity. Arrows point to an example nucleus in each panel.

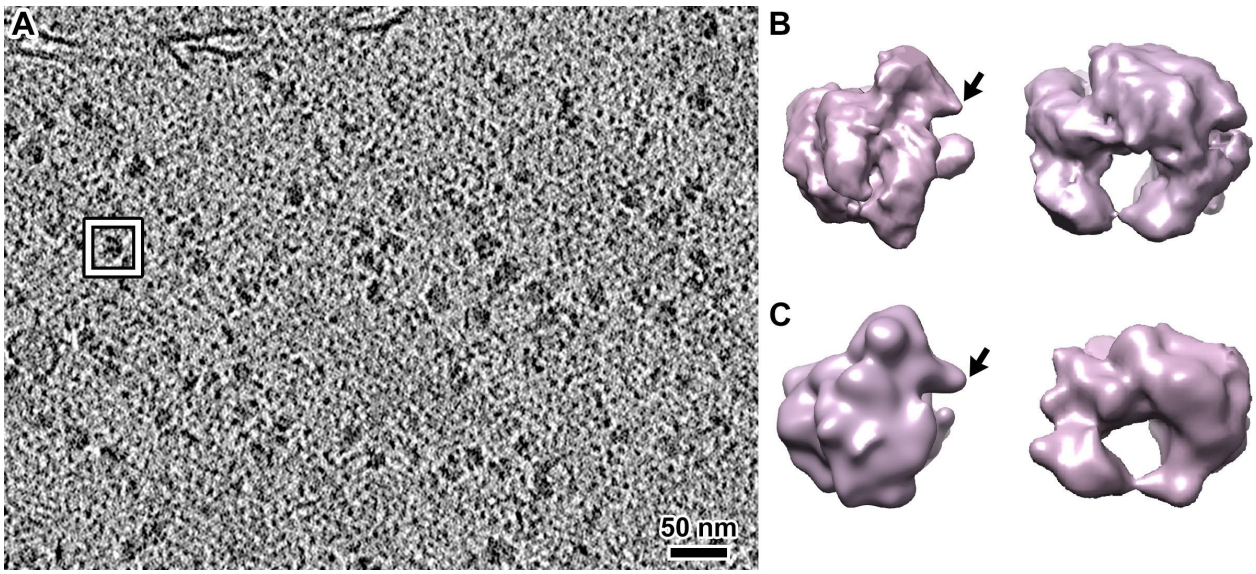

Figure S2. Cryotomograms reveal molecular detail *in vivo*.

(A) Cryotomographic slice (25 nm) of a *S. pombe* cytoplasm position that contains many ribosomes, from the cell shown in Fig. 1B and C. (B) Subtomogram average of cytoplasmic ribosomes. (C) Crystal structure of *S. cerevisiae* 80S ribosome (PDB 4V88; (Ben-Shem et al., 2011)), low-pass filtered to 50 Ångstroms resolution. In panels B and C, the left image is related to the right image by a 90° rotation around the vertical axis, followed by a 180º rotation around the horizontal axis. Notice that in the orientation presented on the left, the “beak” motif (arrow) points to the right in both the simulated density map and the subtomogram average, indicating that the cryotomogram has the correct handedness. The two maps are not expected to be identical because the cytoplasmic ribosome map is an average of multiple conformational states.

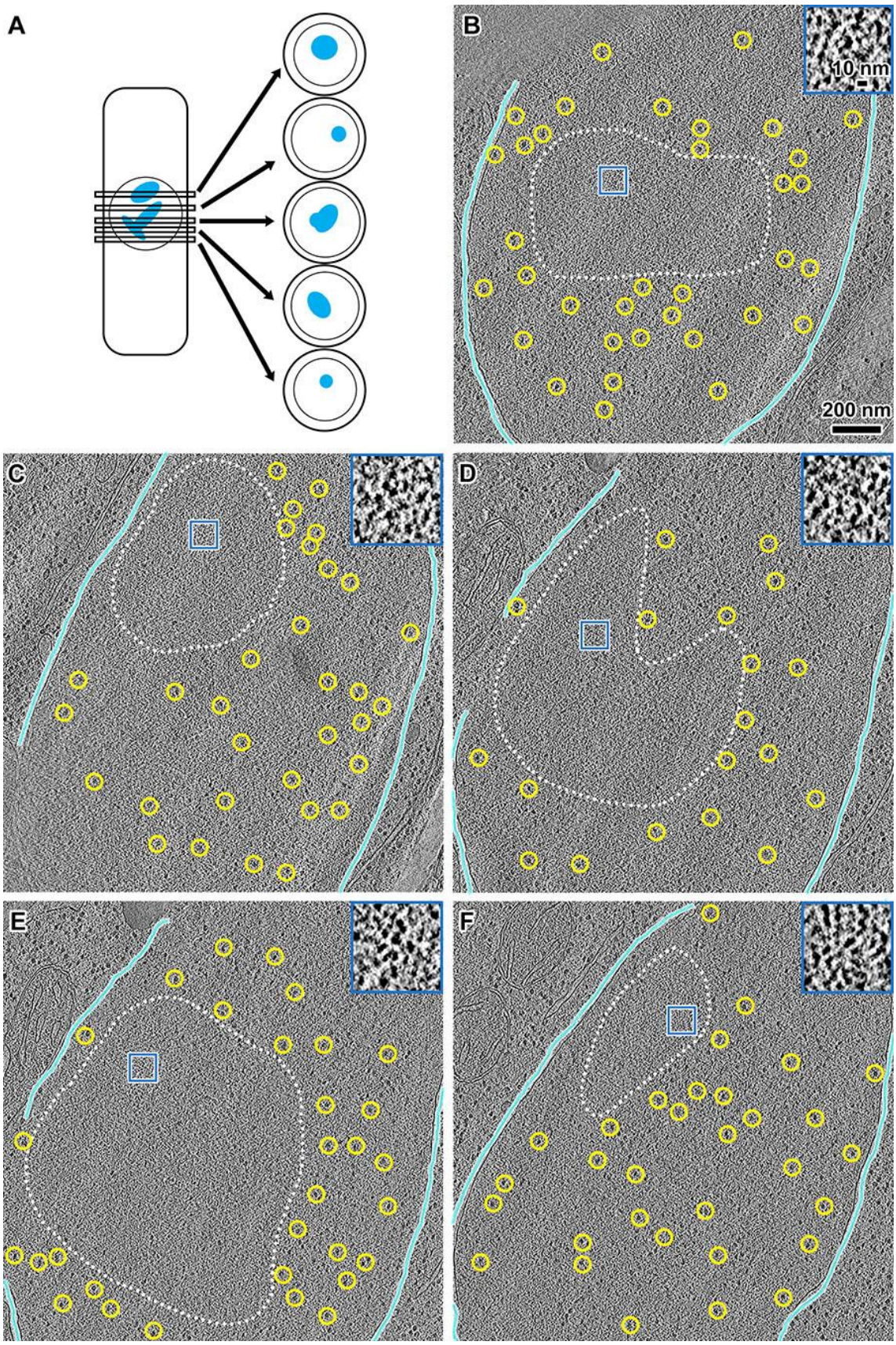

818

819 **Figure S3. Serial cryotomography reveals the location of mitotic chromosomes.**

820 (A) A cartoon showing nearly serial cryosections of a cell. Some cryosections were not

821 imaged due to ice contamination, damage, grid-bar blockage, etc. (B - F)

822 Cryotomographic slices (10 nm) of nearly serial cryosections from a single

823 prometaphase cell. Cyan lines delineate the nuclear envelope; there are gaps where the

824 nuclear envelope densities were ambiguous. Dotted lines: approximate boundaries of

825 condensed chromosomes. Yellow circles: examples of megacomplexes. For clarity, the

826 few megacomplexes inside the dotted lines lines are not annotated. Inset: four-fold

827 enlargements of blue boxes.

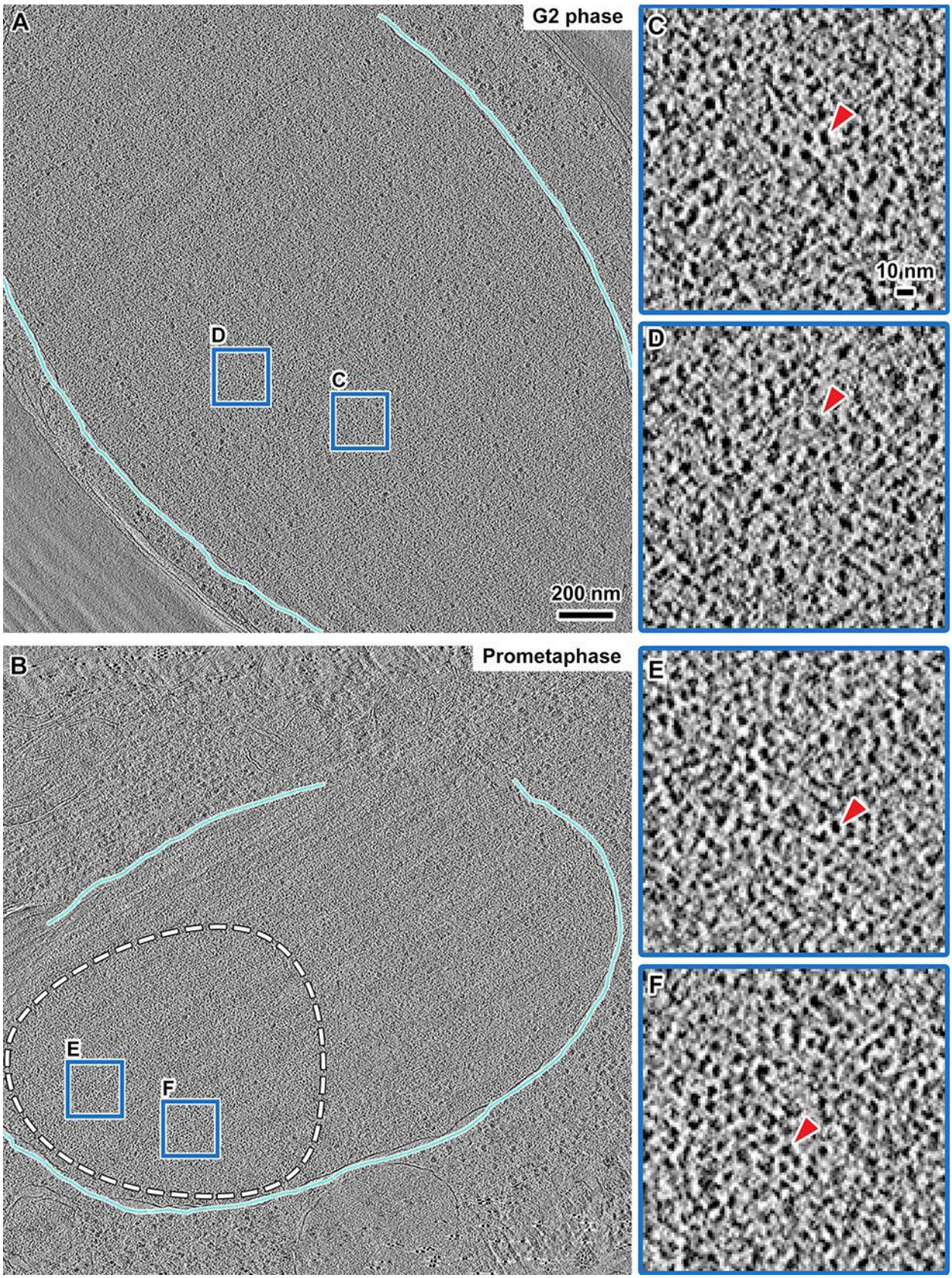

828

Figure S4. An example of nucleosome reorganisation in prometaphase cells.

(A and B) Cryotomographic slices (11 nm) of nuclei in a G2-phase (A) and a prometaphase (B) cell. The cyan lines denote the nuclear envelope; there are gaps where the nuclear-envelope densities were ambiguous. Dashed circle in panel B: approximate outline of a condensed chromosome. (C - F) Six-fold enlargements of intranuclear positions that are enriched in nucleosomes, from the corresponding boxes in panels A and B. Red arrowheads point to nucleosomes.

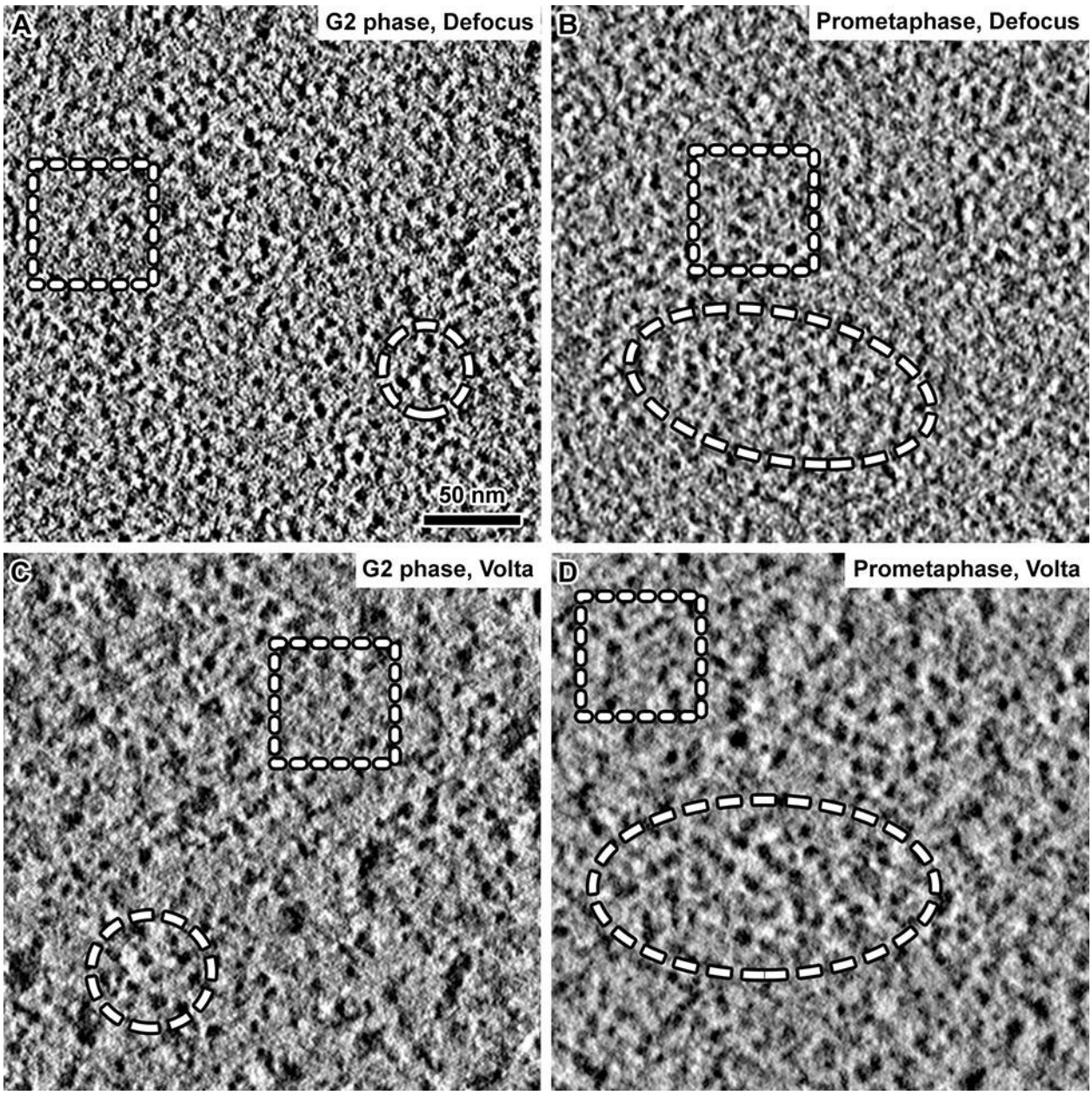

836

837 **Figure S5. Nucleosome reorganisation is distinguishable in both defocus and**

838 **Volta cryotomograms.**

839 (A and C) Cryotomographic slices (10 nm) of positions in G2-phase chromatin imaged

840 with defocus (A) and Volta (C) phase contrast. (B and D) Cryotomographic slices (10

841 nm) of positions in prometaphase chromatin imaged with defocus (B) or Volta (D) phase

842 contrast. Dashed circles: densely packed nucleosomes. Dashed squares: loosely-

843 packed nucleosomes.

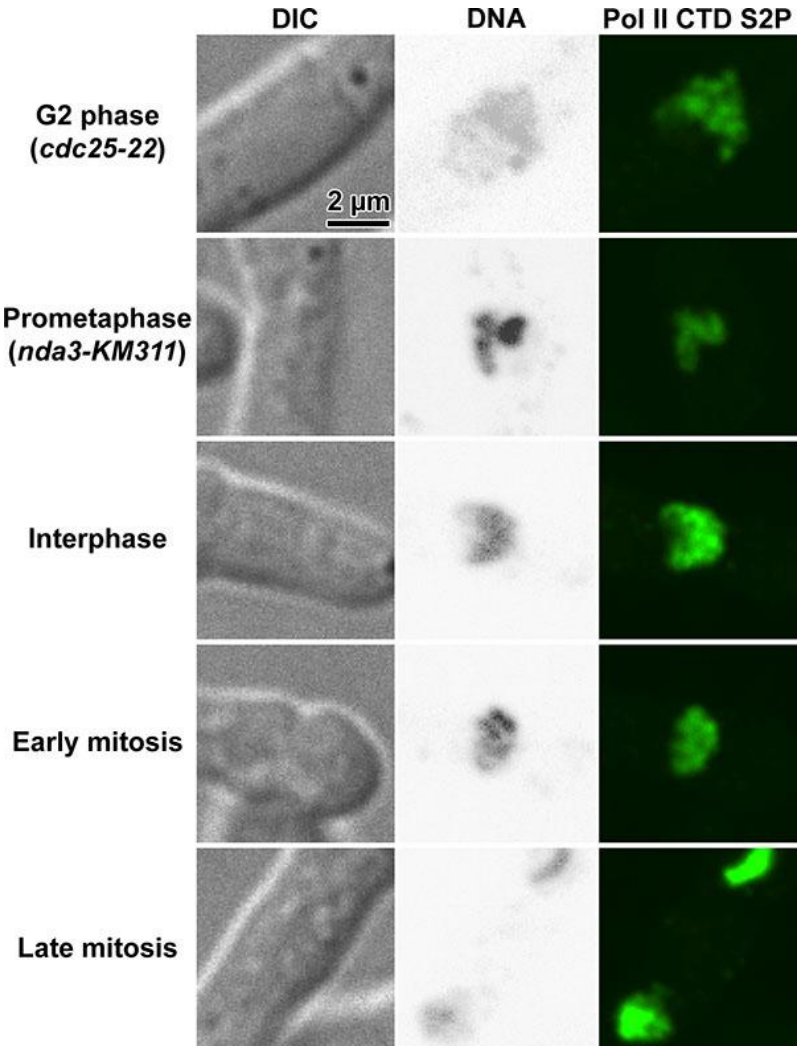

844

845 **Figure S6. Transcription is not completely repressed during mitosis.**

846 DIC and fluorescence images of G2-phase, prometaphase and unsynchronized wild
847 type cells. Left: DIC; Middle: DAPI-stained DNA with inverted contrast; Right:
848 immunofluorescence of RNA polymerase II C-terminal domain repeat, phosphorylated
849 at Serine 2 (Pol II CTD S2P). Top to bottom: *cdc25-22* cell arrested in G2 phase, *nda3-*
850 *KM311* cell arrested in prometaphase, unsynchronized cell in interphase,
851 unsynchronized cell in early mitosis, unsynchronized cell in late mitosis. In the
852 unsynchronized cultures, the cell-cycle states were determined based on the
853 chromosome morphology.

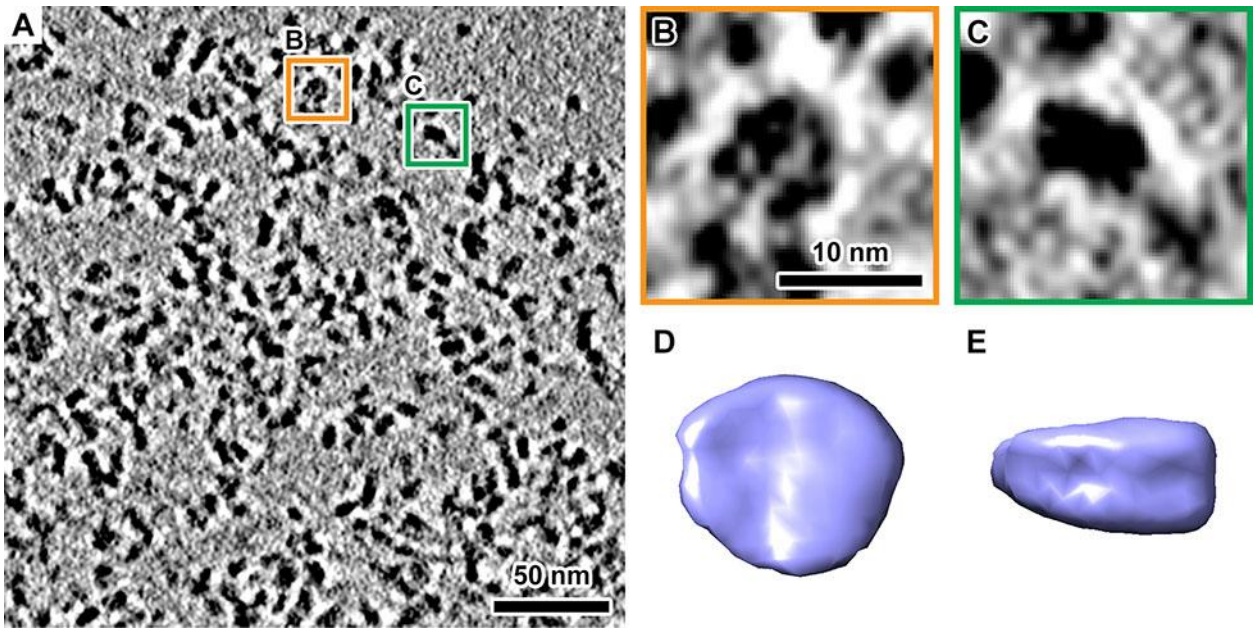

Figure S7. Nucleosomes remain clustered in cell lysates.

(A) Cryotomographic slice (11 nm) showing the chromatin released from unsynchronised *S. pombe* cells. Nucleosomes oriented face-on (orange box) and side-on (green box) are enlarged 5-fold in panels B and C, respectively. (D and E): Face- and side-on views of a nucleosome subtomogram average of particles template-matched from the cryotomogram shown in panel A. Notice that DNA gyres are visible in the side view.

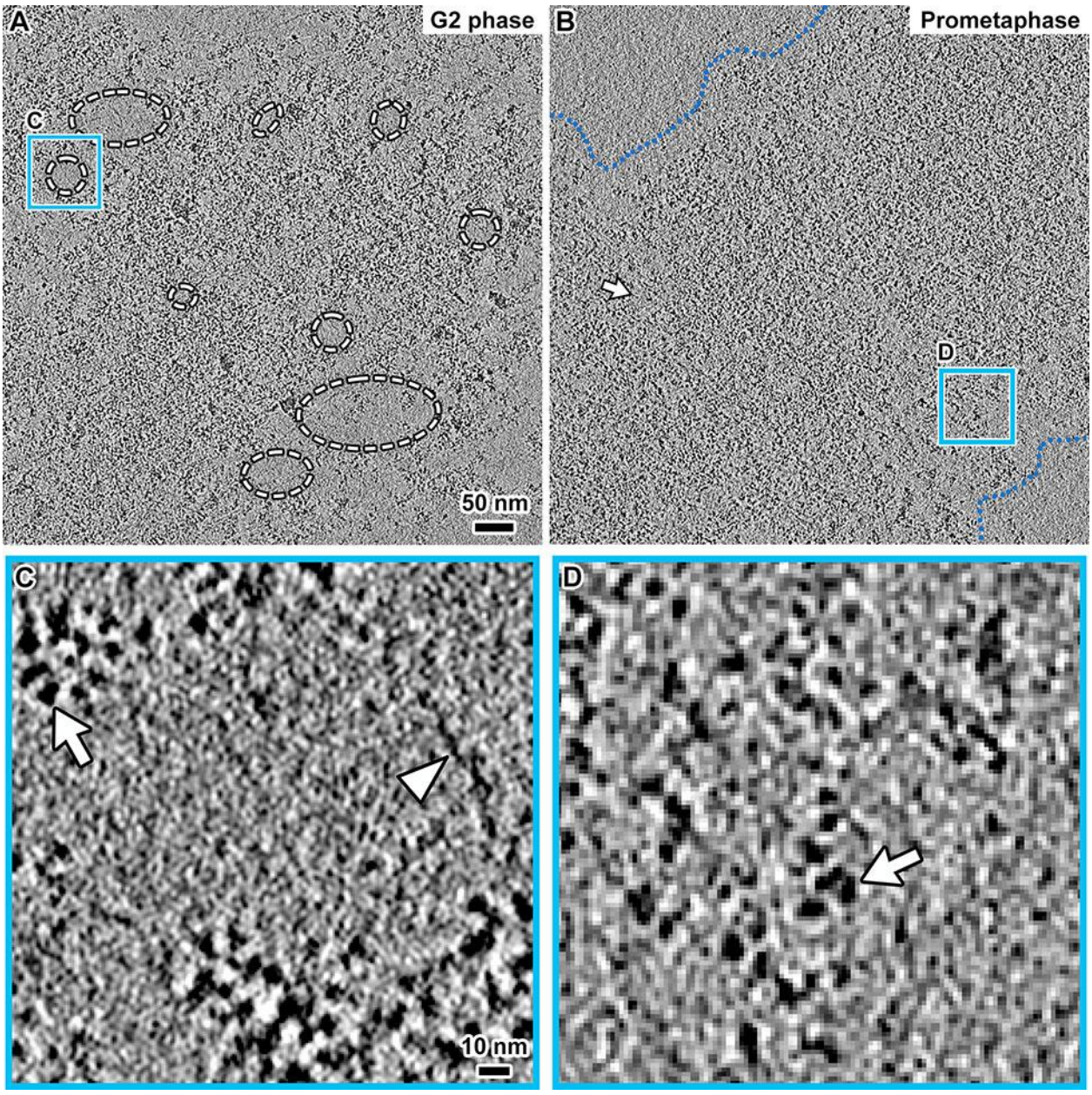

Figure S8. *S. pombe* prometaphase chromatin is also more compact than G2-phase chromatin *in vitro*.

(A and B) Cryotomographic slices (30 nm) of chromatin from G2 phase (A) and prometaphase (B) cell lysates. Dashed circles in panel A: examples of large nucleosome-free gaps. Blue dotted lines in panel B: boundaries of chromatin mass. Arrow in panel B: examples of small nucleosome-free gap. (C and D) Four-fold

869 enlargement of blue boxes in panels A and B, respectively. Arrows: nucleosomes.

870 Arrowhead: DNA.

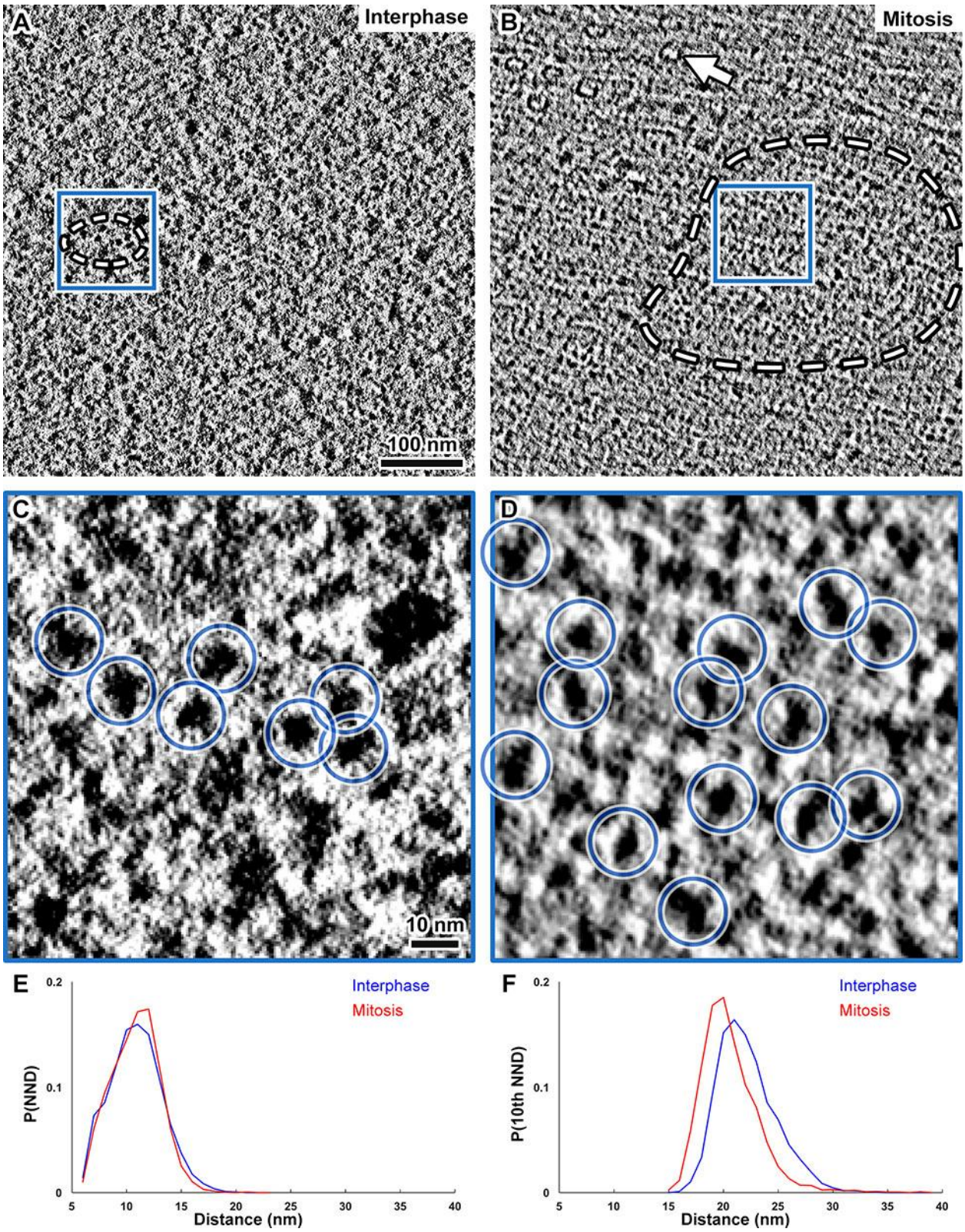

871

872 **Figure S9. *S. japonicus* nucleosomes also pack into larger clusters in mitosis.**

873 (A and B) Volta cryotomographic slices (11 nm) of *S. japonicus* intranuclear positions in
874 an interphase (A) and a mitotic (B) cell. Dashed circles: nucleosome clusters. Arrow in
875 panel B: a spindle microtubule. (C and D) Five-fold enlargements of nuclear positions
876 that have nucleosomes in panels A and B. Nucleosomes are circled in blue. (E)
877 Nearest-neighbor and (F) tenth nearest-neighbor distance analyses of nucleosome
878 template-matching hits.

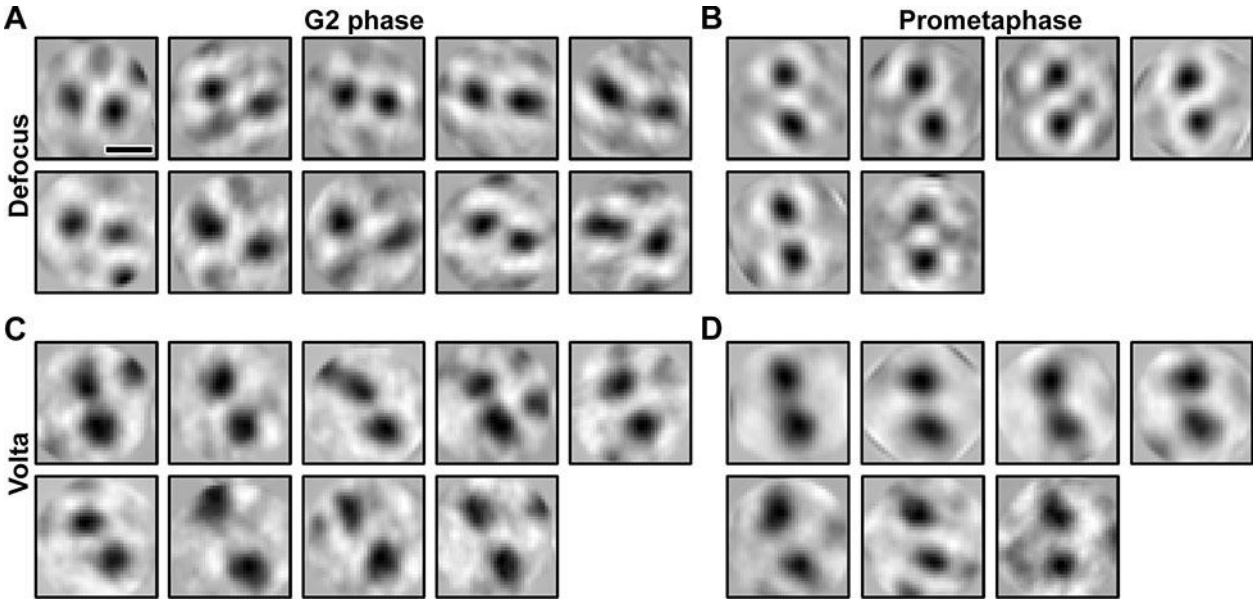

Figure S10. *S. pombe* nucleosomes do not stack face-to-face in either G2-phase or mitotic chromosomes.

(A and C) Two-dimensional classification of dinucleosome template-matching hits in defocus (A) and Volta (C) cryotomograms of G2-phase cells. (B and D) Two-dimensional classification of dinucleosome template-matching hits in defocus (B) and Volta (D) cryotomograms of prometaphase cells. Note that the 2-D classes showing megacomplexes (false positives) or tri-nucleosomes are not shown. Also note that some class averages, e.g., upper-left one in panel A, have a weak third density. This additional density may be from a lower-occupancy nucleosome position or a nucleosome that was truncated by the tomographic slice because it was not in the same exact plane as the other two. Scale bar in panel A: 10 nm.

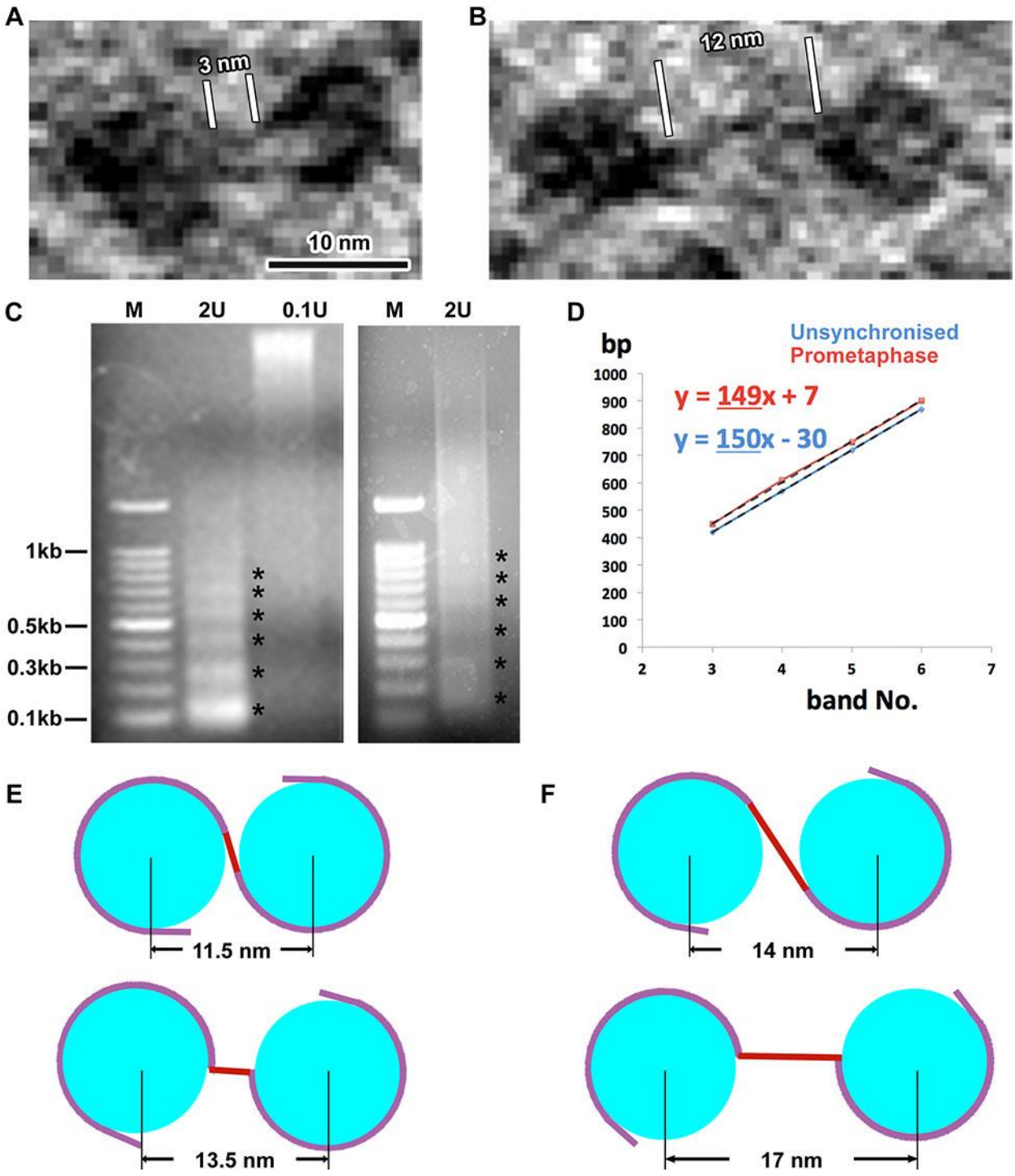

Figure S11. A subset of nucleosomes might be partially unwrapped *in vivo*.

(A and B) Volta cryotomographic slices (10 nm) of a di-nucleosome-like density in a *S. pombe* G2-phase cell, showing densities consistent with short (A) and long (B) linker

DNA. (C) The chromatin in unsynchronised (left; most cells are in G2-phase) and prometaphase (right) cells were fixed and then digested with 2 units or 0.1 units of MNase. DNA bands corresponding to mono- and oligonucleosomes are indicated by asterisks. (D) Nucleosome-repeat length plot of oligomer band number vs. base pairs. The monomer and dimer were excluded from the linear regression because the 'nibbling' of linker DNA at the ends would cause an overestimate of the slope and therefore, the nucleosome repeat length. (E and F) Cartoons showing fully (E) and partially (F) wrapped di-nucleosomes, drawn to scale for the nucleosome diameter and DNA length (but not DNA thickness). Red: *S. pombe* linker DNA. For the fully wrapped nucleosomes, the linker DNA is 2.5 nm (7 bp) long. For the partially wrapped example (10 bp unwrapped from the end of each nucleosome, the linker DNA becomes 6 nm long). The upper and lower panels show the extreme examples that minimize (upper) or maximize (lower) the inter-nucleosome separation for a given linker length. Upper panels: straight linker DNA. Lower panels: linker DNA bent at an energetically unfavorable ring angles at the entry/exit site.

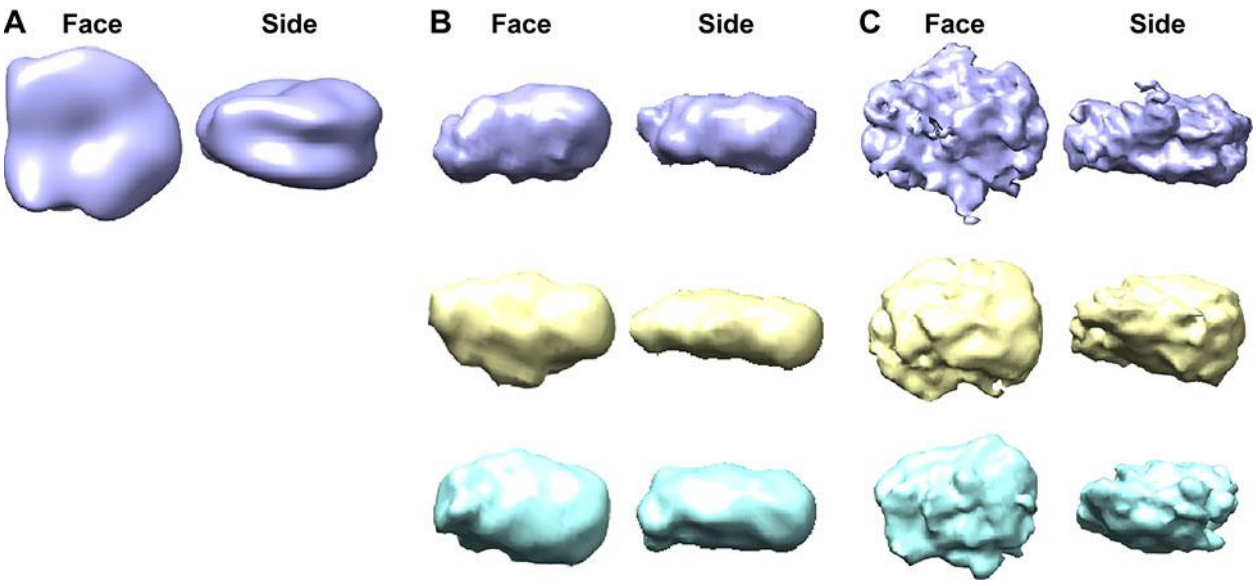

910

911 **Figure S12. 3-D class averages of nucleosome-like densities do not reveal high-**

912 **resolution mononucleosome-like features.**

913 (A) A simulated density map of a mononucleosome crystal structure (PDB 1ID3; (White

914 et al., 2001)), low-pass filtered to 40 Ångstroms resolution. (B and C) Isosurface

915 renderings of representative 3-D class averages of template-matching hits in the nuclei

916 of a defocus (B) and a Volta (C) cryotomogram.

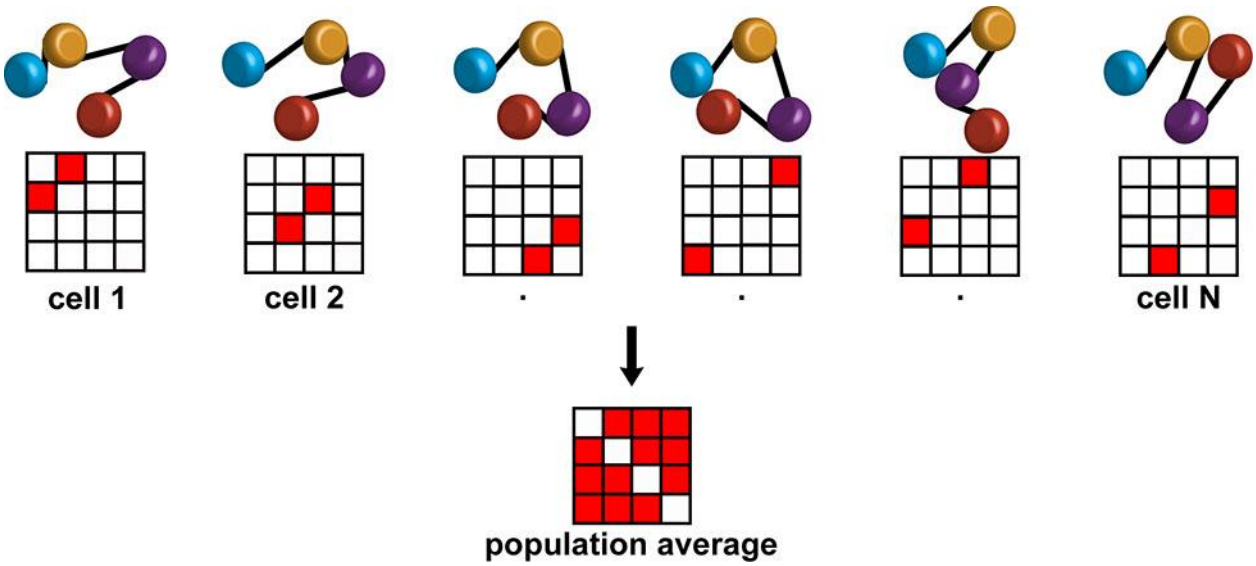

Figure S13. Reconciliation of *S. pombe* cryo-ET and Hi-C chromatin models.

The blue, orange, purple and red rounded cylinders represent four sequential nucleosomes. Black lines indicate the connectivity between nucleosomes. Each column represents the nucleosomal arrangement of a different cell, at the time of fixation. The nucleosome pairs that are in physical contact have the potential to form crosslinks that can result in their detection, which is plotted in the contact matrices in the second row. Cell-to-cell variation at the time of fixation can result in the populational average shown in the Hi-C-based contact map (lower half). For clarity, only four nucleosomes are illustrated, but the concept here scales to clusters containing many more nucleosomes.

927 **Table S1. Cryo-EM and image-analysis specifics.**

EM grid	C-flat 4-2-2, EMS continuous carbon
Microscope	FEI Titan Krios
Energy	300 keV
Gun type	FEG
Camera	Falcon II Direct Detector
Tomography software	Leginon & FEI Tomo
Nominal magnification	8,700, 11000, 18000
Calibrated pixel size	9 Å, 7.3 Å, 4.6 Å
Defocus (nominal)	-8-12 µm
Defocus (fitted)	-9-13 µm
Defocus (nominal, Volta contrast)	-0.5 µm
Cumulative dose	80 - 150 e^- / $Å^2$
Dose fractionation	1 / cosine
Tilt range	±60°
Tilt increment	1° or 2°
Tomogram processing & visualization	IMOD 4.9
Template matching	PEET 1.10 - 1.11
File format conversion	Bsoft 1.8.8
Subtomogram classification & averaging	RELION 1.4, 2.0
Density map visualization	UCSF Chimera 1.11
Figure creation and compositing	Adobe Photoshop and Illustrator CS6, Google sheets

928

929 **Table S2**. Cryotomogram details

Tomogram ID	Cells	Cell-cycle state, sample type	Figure	Dose	Pixel size (Å)	Defocus † (μm)		DPC/ VPC
						nom	ref	
15Jun11_03	*pombe*	G2, cell	1B, C, S2	103	7.3	12	13-17	DPC
17May10_01	*pombe*	G2, cell	2, S5A, S10A	80	7.3	12	13	DPC
17May09_18	*pombe*	PM, cell	3	80	7.3	12	12	DPC
15Nov16_10	*pombe*	PM, cell	4, 5B, D	100	4.6	0.5		VPC
16Mar19_123	*pombe*	G2, cell	5A, C, S12	100	4.6	0.5		VPC
16Dec21_20	*pombe*	PM, cell	S3B	150	7.3	12	13	DPC
16Dec21_18	*pombe*	PM, cell	S3C	150	7.3	12	13	DPC
16Dec21_13	*pombe*	PM, cell	S3D	150	7.3	12	13	DPC
16Dec21_12	*pombe*	PM, cell	S3E	150	7.3	12	13	DPC
16Dec21_06	*pombe*	PM, cell	S3F	150	7.3	12	13	DPC
15Jun11_07	*pombe*	G2, cell	S4A, C, D	103	7.3	12	13-17	DPC
15May25_02	*pombe*	PM, cell	S4B, E, F	100	7.3	12	10-17	DPC
17May09_13	*pombe*	PM, cell	S5B, S10B	80	7.3	12	13	DPC
17May10_02	*pombe*	G2, cell	S5C, S10C	80	7.3	0.5		VPC

16Dec06_10	*pombe*	PM, cell	S5D	150	7.3	0.5		VPC
16Nov14_05	*pombe*	Unsynchronised, lysate	S7	150	7.3	12	12	DPC
17Jul08_04	*pombe*	G2, lysate	S8A, C	108	7.3	12	14	DPC
17Jul08_01	*pombe*	PM, lysate	S8B, D	100	7.3	12	14	DPC
16Aug12_03	*japo*	Interphase, cell	S9A, C	100	5.8	0.5		VPC
16Jul25_14	*japo*	Mitosis, cell	S9B, D	100	7.3	0.5		VPC
16Dec06_7	*pombe*	PM, cell	S10D	150	7.3	0.5		VPC
15Nov16_09	*pombe*	G2, cell	S11A, B	100	4.6	0.5		VPC

930 Cell type: *pombe* = *S. pombe*; *japo* = *S. Japonicus*, G2 = G2 phase, PM =

931 prometaphase, Dose, in electrons / $Å^2$; † Nominal (nom) and refined (ref) defocus

932 values; DPC = defocus phase contrast; VPC = Volta phase contrast